

# Dynamics of cooperative excavation in ant and robot collectives

S Ganga Prasath<sup>1†</sup>, Souvik Mandal<sup>2,3†</sup>, Fabio Giardina<sup>1†</sup>, Jordan Kennedy<sup>1</sup>, Venkatesh N Murthy<sup>2,3</sup>, L Mahadevan<sup>1,3,4,5</sup>

\*For correspondence:  
lmahadev@g.harvard.edu (LM)

†These authors contributed  
equally to this work

<sup>1</sup>School of Engineering and Applied Sciences, Harvard University, Cambridge, United States; <sup>2</sup>Department of Molecular and Cellular Biology, Harvard University, Cambridge, United States; <sup>3</sup>Center for Brain Science, Harvard University, Cambridge, United States; <sup>4</sup>Department of Physics, Harvard University, Cambridge, United States; <sup>5</sup>Department of Organismic and Evolutionary Biology, Harvard University, Cambridge, United States

**Abstract** The solution of complex problems by the collective action of simple agents in both biologically evolved and synthetically engineered systems involves cooperative action. Understanding the resulting emergent solutions requires integrating across the organismal behaviors of many individuals. Here we investigate an ecologically relevant collective task in black carpenter ants *Camponotus pennsylvanicus*: excavation of a soft, erodible confining corral. Individual ants show a transition from individual exploratory excavation at random locations to spatially localized collective exploitative excavation and eventual excavate out from the corral. An agent minimal continuum theory that coarse-grains over individual actions and considers their integrated influence on the environment leads to the emergence of an effective phase space of behaviors in terms of excavation strength and cooperation intensity. To test the theory over the range of both observed and predicted behaviors, we used custom-built robots (RAnts) that respond to stimuli to characterize the phase space of emergence (and failure) of cooperative excavation. By tuning the amount of cooperation between RAnts, we found that we could vary the efficiency of excavation and synthetically generate the other macroscopic phases predicted by our theory. Overall, our approach shows how the cooperative completion of tasks can arise from simple rules that involve the interaction of agents with a dynamically changing environment that serves as both an enabler and a modulator of behavior.

## Introduction

Collective behavior is seen in organisms across many decades in length-scale, from the microscopic to the macroscopic (Nowak, 2006; Camazine et al., 2020; Gordon, 1999; Seeley, 2009; Couzin et al., 2003). These behaviours are often functional and serve as solutions to problems associated with a range of tasks that cannot be solved efficiently at the individual level: from brood care to foraging for food, protection from enemies and predation of prey, building complex architectures etc. (Feinerman et al., 2018; Ocko and Mahadevan, 2014; Hölldobler et al., 2009; Peleg et al., 2018; Rasse and Deneubourg, 2001). Since collective behavior involves multiple individuals, it necessarily involves some form of communication and/or cooperation that takes different forms across scales - from quorum sensing in unicellular bacterium and slime molds, to the waggle dance in bees, and various forms of physical signal propagation in animal societies and human organizations (Rasse and Deneubourg, 2001; Alcock, 2001; Pennisi, 2009; Nowak, 2006; Elster et al., 1998; Couzin et al., 2003).

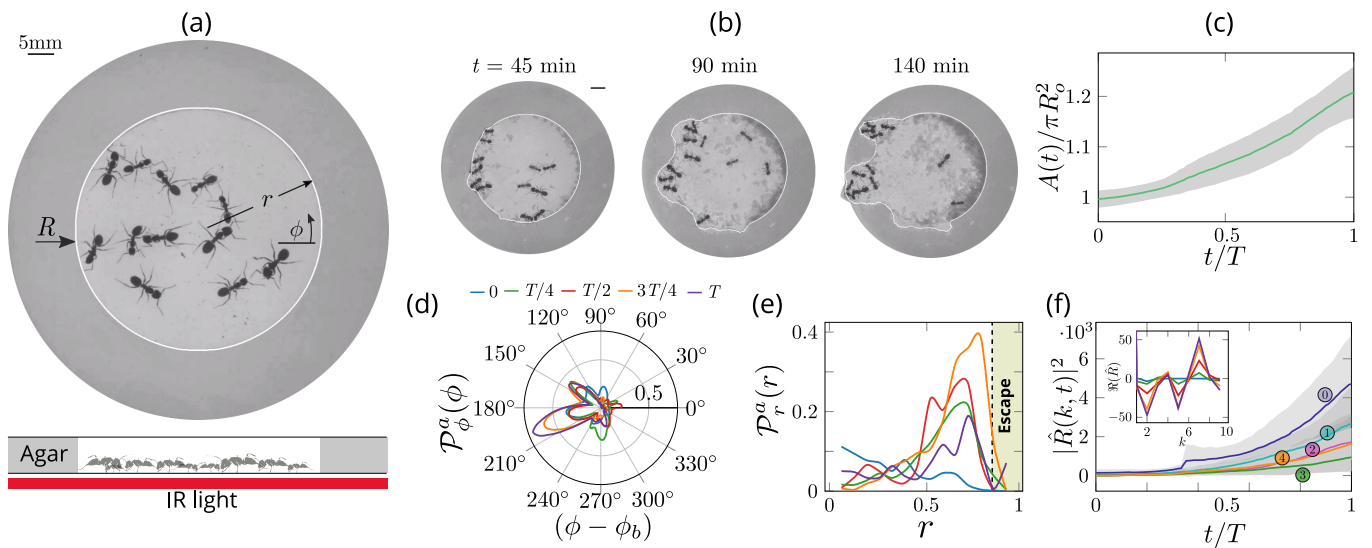


**Figure 1. Collective dynamics of ant excavation** (a) Colony members of the black carpenter ant *Camponotus pennsylvanicus* are confined to a porous boundary made out of Agarose. The boundary is represented by its radius  $R(\phi, t)$  ( $\phi$  - polar angle,  $t$  - time). Bottom part shows the side-view schematic of the experimental set-up with the boundary made of agarose and background IR light source used to image the ants in the dark. (b) Temporal progression of excavation experiments as 12 ants cooperatively tunnel through the agarose confinement. The white line is the tracked location of the inner wall which grows in size as the excavation progresses. (c) Confinement area  $A(t)$  as a function of time (scaled by time to excavate out of the corral  $T$ ), normalized by initial circular confinement with radius  $R_0$ . (d) Evolution of the orientation distribution of the ant density,  $\mathcal{P}_\phi^a(\phi, t)$  obtained by averaging along the radial direction. Ants start from an initially isotropic state and localize at an angle  $\phi_b$  along the boundary.  $T$  here is the excavation time. (e) Dynamics of the radial distribution of ant density  $\mathcal{P}_r^a(r, t)$  as a function of radial distance,  $r$  obtained by averaging a sector of  $\pi/6$  around the excavation site. We see that the ant density front propagates through the corral. The density is plotted for the same times as in (d). (f) Evolution of the power spectrum  $|\hat{R}(k, t)|^2$  of first five Fourier modes capturing the number of tunnels formed during excavation  $R(\phi, t) = \sum_k \hat{R}(k, t)e^{ik\phi}$ . Inset shows the real part of the Fourier coefficient,  $\Re(\hat{R})$  at different time instants indicating that many modes are present in the boundary shape.

42 The importance of environmental signals is particularly clearly seen in examples of collective  
 43 task execution in social insects that have a long history of documented cooperative behavior (*Hölldobler et al., 1990; Gordon, 1999; Perna and Theraulaz, 2017; Mikheyev and Tschinkel, 2004*).  
 44 Super-organisms made of individuals that respond to local stimuli with stereotypical actions that  
 45 leave their "mark" on the environment, creating a spatio-temporal memory, and is commonly  
 46 known as stigmergy (*Hölldobler et al., 2009*). While stigmergy is usually associated with scalar  
 47 pheromone fields, a broader definition might include the use of signaling via chemical, mechanical  
 48 and hydrodynamic means (*Buhl et al., 2005; Mikheyev and Tschinkel, 2004*), as has been quanti-  
 49 fied in recent studies of bees (*Ocko and Mahadevan, 2014; Peleg et al., 2018*). To understand how  
 50 collective task execution arises, we need to understand how individuals switch from local uncoor-  
 51 dinated behavior to collective cooperation that translates to successful task execution in different  
 52 social systems. From a biological perspective, this naturally involves understanding the neural cir-  
 53 cuits, physiology and ethology of an individual. A complementary perspective at the level of the  
 54 collective is that of characterizing a "crude view of the whole," which entails the quest for a small  
 55 set of rules that are sufficient for task completion and the range of possible solutions that arise  
 56 from these rules that might be tested experimentally. And finally, given the ability to engineer min-  
 57 imally responsive biomimetic agents such as robots (*Rahwan et al., 2019*), a question that suggests  
 58 itself is that of the synthesis of effective behaviors using these agents. Therefore, we also explore  
 59 regions of phase space that are hard to explore with social insects, to learn about the robustness  
 60 of these behaviors using imperfect agents in uncertain and noisy physical environments, before  
 61 looking for them *in-vivo*.  
 62

63 Here we use an ecologically relevant task in carpenter ants *Camponotus Pennsylvanicus*: exca-  
 64 vation and tunneling, to quantify the dynamics of successful task execution by tracking individual  
 65 ants, use this to create a quantitative framework that takes the form of mathematical models for

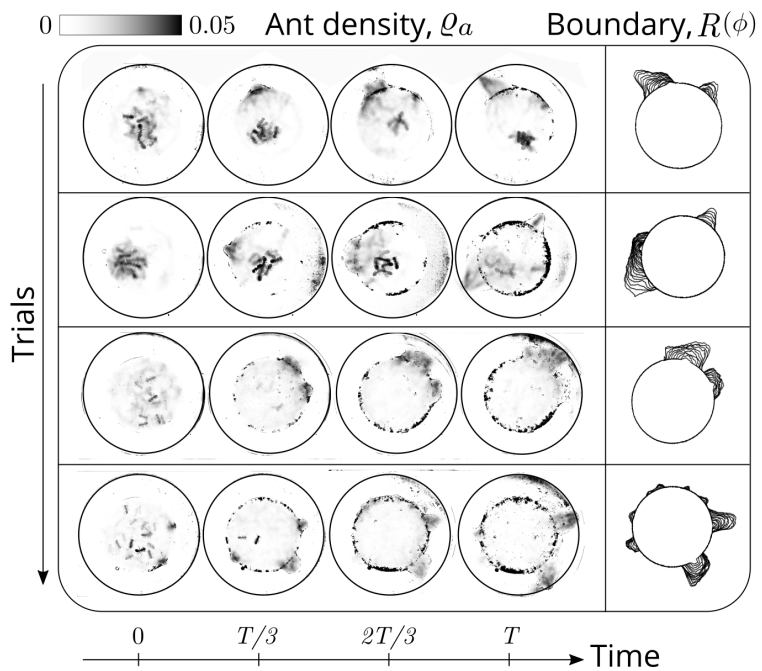


**Figure 2.** Evolution of the ant density field,  $\rho_a(\mathbf{x}, t)$  (in units of  $\#/mm^2$ ) as the tunneling progresses for experiments with 12 major ants. The density field is obtained by averaging the ant locations over 250 secs during the tunneling process. In the second columns is the evolution of the boundary shape,  $R(\phi)$  as a function of time where we see multiple excavation sites being explored before one of them succeeds. The darker spots in the image are the debris that the ants deposit as they excavate the boundary.

66 the behavior of how agents communicate and cooperate, and finally synthesize the behavior using  
 67 robots that can sense and act. Our work complements and builds on earlier studies on excavation  
 68 (*Buhl et al., 2005; Tschinkel, 2004; Deneubourg and Franks, 1995; Deneubourg et al., 2002*) in  
 69 social insects that looked at the effects of population size and role of cooperation on efficiency of  
 70 digging and developed 1-dimensional models to understanding the effective excavation process.  
 71 We go beyond these studies by (i) quantifying the collective behavior of ants by tracking them in  
 72 space-time while following the dynamics of how they interact with each other and the simultaneous  
 73 excavation a substrate that confines them, and (ii) use our observations to develop a theoretical  
 74 framework that couples the change in ant density, substrate density and the rate of antennation in  
 75 space and time to capture the collective execution of the task. We also identify the non-dimensional  
 76 parameters that define the range of behaviors of the agents and use this to map out the dynamics  
 77 of agents in different phases using an agent-based model. (iii) We then synthesize and recreate  
 78 this behavior using custom-built robots that can respond to each other and the environment to  
 79 show how they can perform this collective task. An important outcome of our study is a phase  
 80 diagram that shows the emergence of different collective behaviors associated with task comple-  
 81 tion as a function of just two dimensionless parameters that characterize the local rules underlying  
 82 individual behavior and the nature of communication between agents, e.g. ants and robots.

### 83 **Materials and methods**

#### 84 **Excavation in Carpenter ants**

85 We start with ants drawn from a mature colony of *C. Pennsylvanicus* that consist of a queen, the  
 86 sole egg layer, and the workers from three morphologically different castes - major, median and  
 87 minor (*Hansen and Klotz, 2005*). Though all ants perform different tasks like foraging, nest-keeping,  
 88 brood care to a varied degree, during excavation, major ants, equipped with their large mandibles,  
 89 generally take the lead role, while media and minor ants transport the debris outside their nest.  
 90 Ants communicate primarily through their antennae by using them to sense pheromones released

91 by other ants and by touching other ants to identify their caste. It is this inter-organismal informa-  
 92 tion exchange that enables the collective solution of complex tasks. Our experiments consist of a  
 93 dozen worker ants from the same colony that are anesthetized (using  $CO_2$ ) and then brought into a  
 94 confining corral made out of agarose flanked between two hard plastic sheets, without visible light  
 95 to mimic their natural environment in a nest; infrared light was used to monitor the experiment  
 96 using video (see **Figure 1(a)**). We used a ring-like confinement made of agarose gel, with a height  
 97 of 10 mm, an inner radius of 35 mm and outer radius of 55 mm, making the ring 20 mm thick. We  
 98 performed a total of 7 sets of experiments with 4 experiments with a collective of 12 majors ants  
 99 and 3 sets of experiments with a mixture of 4 major, 4 media and 4 minor ants. Once the ants  
 100 regain activity (due to the introduction of  $O_2$ ), they stay still for a while before moving. Observa-  
 101 tions show that they first exhibit wall-following followed by one of the ants initiating an exploratory  
 102 excavation at a random location along the corral (ref **Figure 2**). After an initial exploratory phase  
 103 the ants switch to an exploitative strategy in which they excavate a tunnel at a specific location and  
 104 eventually break through the corral (see the sequence in **Figure 1(b)**).

105 We can quantify this transition from rotationally isotropic exploration to localized excavation by  
 106 considering either the behavior of individual ants or their effective density  $\rho_a(r, \phi, t)$  as a function of  
 107 the polar coordinates  $(r, \phi)$  and time. We choose to use an effective coarse-grained density for two  
 108 reasons: it is a more natural variable in the limit of large populations that vary in space and time,  
 109 and is also amenable to building effective theories to which experiments can be compared. The  
 110 ant density is obtained by averaging the position of the ants over a time window larger than the  
 111 time taken for them to perform one cycle of excavation at the boundary to dropping debris in the  
 112 bulk (see sec. 1 for further details). Over time, the density becomes localized at a particular angle  
 113 and location along the corral where large-scale excavation eventually leads to excavation out of  
 114 the corral (see Video 3, **Figure 2** and SI **Figure 1** for the coarse-grained spatio-temporal evolution  
 115 of the ant density, obtained by this averaging procedure). Simultaneously, we see a signature of  
 116 collective excavation in an increase of the volume of excavated material, as shown in **Figure 1(c)**  
 117 (see also (**Toffin et al., 2009**)). Averaging the density over radial positions, in **Figure 1(d)** we show the  
 118 orientation distribution of the ant density  $\mathcal{P}_\phi^a(\phi, t) = \int \rho_a(r, \phi, t) dr$  is initially isotropic, and gradually  
 119 starts to localize at a particular (arbitrary) value of the angle as time increases.

120 Averaging the density over the localized region, in **Figure 1(e)** we show the radial distribution of  
 121 the ant density  $\mathcal{P}_r^a(r, t) = \int \rho_a(r, \phi, t) S(\phi) d\phi$  (where  $S(\phi)$  is a kernel around the excavation site) that  
 122 is initially uniform, and gradually propagates inside the boundary of the corral as time increases.  
 123 Consistent with localization and concomitant excavation (**Figure 1(f)** inset, SI **Figure 2(c)**), we see  
 124 that the Fourier amplitudes of multiple modes compete with each other initially before an elliptic  
 125 mode (corresponding to a strongly localized state) is amplified as excavation progresses (shown in  
 126 **Figure 1(f)**, SI **Figure 2(b)**). All together, our quantitative observations show that an initially isotropic  
 127 and homogeneous distribution of ants in the corral induces exploration of multiple potential tun-  
 128 neling paths that transitions into the exploitative excavation of one specific location that eventually  
 129 leads to an excavation route.

### 130 **Model of cooperative excavation**

In order to understand the dynamics of this cooperative excavation we model the ants using dis-  
 crete agents that mimic the microscopic behaviors of ants and also obtain a coarse-grained field  
 model for their evolution by averaging over the local actions. In the 2-dimensional agent-based  
 model each ant is represented as a circular disk of radius  $a$  with center position  $\mathbf{r}_j(t)$  and orientation  
 $\hat{\mathbf{p}}_j(t)$  where  $j = 1 \dots n$ ,  $n$  being the number of ants in the domain (see **Figure 3(a)**). We approximate  
 the confining corral in the experiments using discrete boundary elements which the agents can  
 pick and place in the interior of the domain (see **Figure 3(b)**). The agents engage in exploration  
 within the corral in the absence of external gradients, consistent with observations (**Trible et al.,**  
**2017**) and their motion is rectified either by the presence of pheromone gradients or reinforcing  
 antennating signals (**Hölldobler et al., 1990; Reinhard and Srinivasan, 2009; Waters and Bassler,**

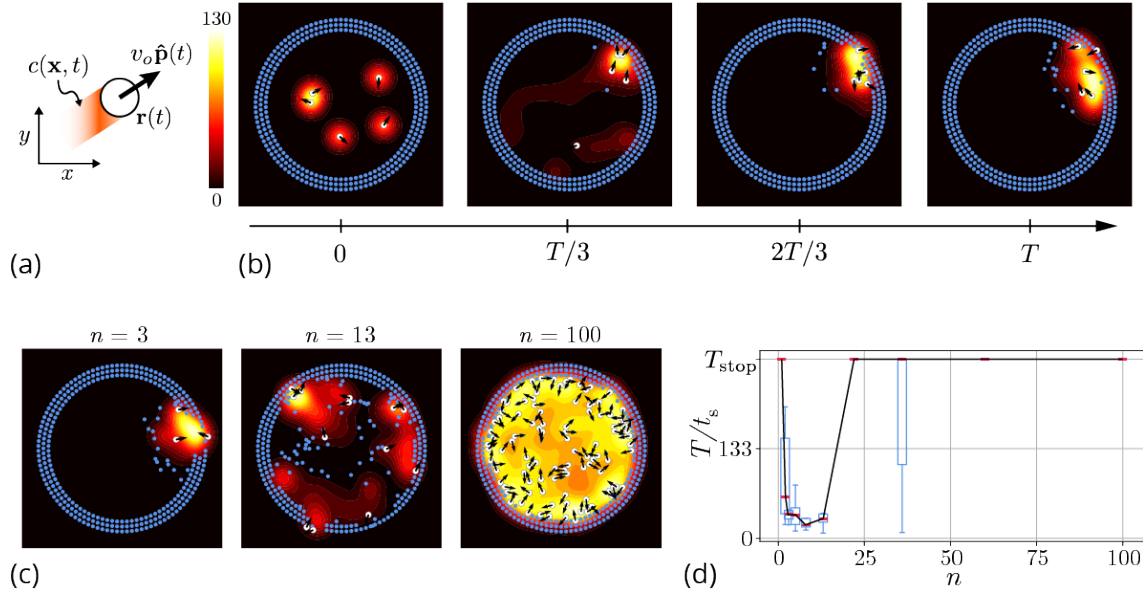


**Figure 3. Agent-based simulation** (a) Schematic of the agents in our simulation captured by their position  $\mathbf{r}(t)$  and orientation  $\hat{\mathbf{p}}(t)$  moving at speed  $v_o$ . These agents generate an antennating field  $c(\mathbf{x}, t)$  at a constant rate  $k_+$  which decays at a rate  $k_-$ . (b) Progression of cooperative excavation of the corral by 5 agents as they pick elements from the boundary and drop them in the interior (see sec. [Table 1](#) for parameters). Color bar shows the magnitude of antennating field and it varies between 0-130. (c) Snapshot of the dynamics at the end of simulations corresponding to  $T_{\text{stop}} = 266$  for the number of agents  $n = 3, 13, 100$ . We see that agents can go from excavating successfully to being trapped in their own communication field. (d) Box plot showing the time taken to excavate out of the corral  $T/t_s$  (non-dimensionalized using  $t_s$  - time taken for an agent to travel the entire domain) as a function of the number of agents  $n$  in the corral when  $T_{\text{stop}} = 266$ . For very small and very large number of agents the collective does not excavate out as the median  $T/t_s = T_{\text{stop}}$  and they escape fastest for  $n = 8$ .

[2005; Gordon et al., 1993; Hillen and Painter, 2009; Toffin et al., 2009](#)). This is because communication between ants is mediated either via antennation and/or pheromones which act as two different modes of information transfer. The former involves information moving with the ants and the latter leads to changes in the fixed environment. However, when ants move slowly relative to the time for the decay of the memory associated with antennation with other ants, the dynamics of both these processes is similar. Then the signals laid down (or transported) by ants increases locally at a rate proportional to their density ([Gordon, 2021](#)), and is subject to degradation and diffusion slowly. Accounting for these effects, we arrive at the following dynamical equations for the evolution of  $\mathbf{r}_j(t), \theta_j(t), c(\mathbf{x}, t)$ :

$$\dot{\mathbf{r}}_j(t) = \underbrace{v_o \hat{\mathbf{p}}(t)}_{\text{Self-propulsion}}, \quad (1)$$

$$\dot{\theta}_j = \underbrace{G \nabla_{\perp} c}_{\text{Antennation feedback}} + \underbrace{\eta_j(t)}_{\text{Exploration}}, \quad (2)$$

$$\partial_t c = \underbrace{D_c \nabla^2 c}_{\text{Diffusion}} + \underbrace{k_+ \sum_{j=1}^n \mathcal{H}(\mathbf{r}_j(t); a)}_{\text{Production}} - \underbrace{k_- c}_{\text{Decay}}. \quad (3)$$

131 Here the orientation of the agents is given by  $\hat{\mathbf{p}}_j = (\cos \theta_j, \sin \theta_j)$  with  $\theta_j$  being the heading an-  
 132 gle,  $v_o$  the characteristic speed of the agents,  $\eta_j$  is a Gaussian white noise with correlation function  
 133  $\langle \eta_j^k(t) \eta_j^l(t') \rangle = 2D_a \delta_{k,l} \delta(t - t')$ . Further the agents produce antennating field at a rate  $k_+$  which  
 134 decays at a rate  $k_-$ . Here the production of the antennating field is captured by a square function  
 135  $\mathcal{H}(\mathbf{r}_j, a) = \{1 \text{ if } |\mathbf{x} - \mathbf{r}_j|^2 - a^2 \leq 0; 0 \text{ if } |\mathbf{x} - \mathbf{r}_j|^2 - a^2 > 0\}$ . We assume that the gradient in the antennating  
 136 field along the local normal determines the rotation of the agents by a magnitude  $G$  is the rotational  
 137 gain. In order for the agents to initiate the excavation process, they can pick the elements from

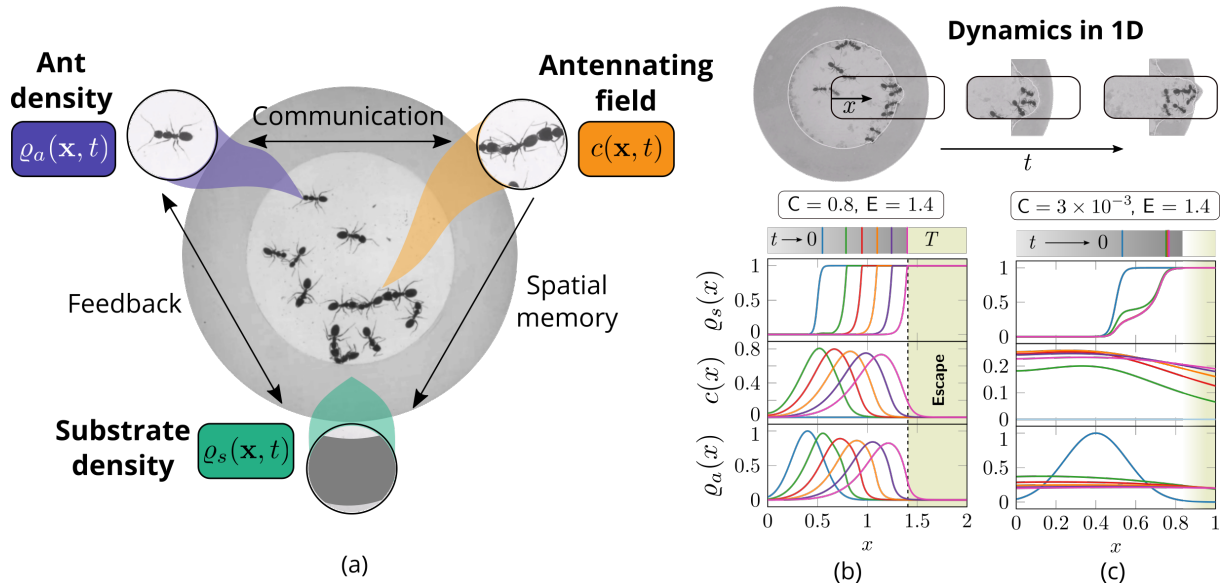


**Figure 4. Cooperation via organism-environment-organism interaction** (a) Schematic of the model showing the interaction between the different spatio-temporal fields required to capture cooperative excavation of ants: ant density,  $\rho_a(\mathbf{x}, t)$ ; concentration of antennating field,  $c(\mathbf{x}, t)$  capturing inter-ant communication; density of corral,  $\rho_s(\mathbf{x}, t)$  representing the soft corral which the ants excavate. We capture the dynamics of excavation by ants close to the excavation site using the 1-dimensional version of *Equation 4-Equation 5*. (b, c) Temporal progression of the corral density, antennating field and the ant density showing successful excavation for high cooperation captured using the non-dimensional number,  $C$  (representing non-dimensional strength of cooperation amongst ants) and faster excavation, captured using  $E$ . For reduced cooperation ants' diffusion dominates and only partial tunnels are formed (see SI 2 for details).  $T$  here is the time for excavating out of the corral. The agent density is a gaussian function centered around  $x = 0.5$ .

138 the boundary and drop them in the interior of the corral only when the local concentration of the  
139 antennating field is beyond a critical threshold  $c^*$  ensuring that the agents start performing a task  
140 only after enough number of interactions among themselves, consistent with observations (**Gor-**  
141 **don, 2021; Gordon et al., 1993**). **Figure 3(b)** shows snapshots of simulation following the dynamics  
142 of **Equation 1-Equation 3** where the agents excavate successfully out of the corral when we ensure  
143 that the gradient following behavior is strong (see SI 2 for details). Given such a dynamics, we ex-  
144 pect the time taken to excavate out of the corral is going to be a function of the number of agents.  
145 In order to characterize the behavior we vary the number of agents from  $n = 1 - 100$  and find that  
146 for very small or large number of agents in the corral, the agents do not excavate out during the  
147 time of simulations,  $T_{\text{stop}}$  (see **Figure 3(c, d)**), seen as saturation in the excavation time  $T/t_s$ .

In the agent based simulations we can encode the behavior of ants with all its details such as prescribing the sequence of actions taken during the execution of pick and place task, the path taken during the dropping of debris in the interior of the coral, changes in orientation after inter-ant interaction and so on. It also helps us get an estimate time of excavation given these behavioral rules. Further, as we have seen, we can study the effect of number of agents on the time of excavation. However for each of these actions there is a parameter associated with it in the simulations which results in a large dimensional phase-space. These simulations, moreover, are computationally expensive as one needs to couple the antennating field equations (which is a partial differential equation) with discrete agents and also evaluate the mutual interaction of all the agents in the corral. In order to gain insights into the relevant parameters that describe our observations in the agent-based model and also the parameters that govern the macroscopic dynamics of the collective, we develop a theoretical framework that coarse-grains over the fast times and short length scale actions of the agents, i.e. considers spatial variations over scales much larger than a "mean-free path" and "collision time" associated with agent-agent interactions. A formal coarse-graining of the actions from the discrete agent-based simulations to the continuum is often difficult and one resorts to closure models to account for the effects of fluctuations accurately. Our effec-

tive theory attempts to couple three slowly-varying spatio-temporal fields: the ant density  $\rho_a(\mathbf{x}, t)$ , a communication field  $c(\mathbf{x}, t)$  representing processes such as antennation and pheromone-based communication that the ants use to communicate with each other, and the corral density  $\rho_s(\mathbf{x}, t)$ , shown schematically in **Figure 4(a)** to explain our observations in terms of a small number of effective measurable parameters. In the continuum picture, the agents' random motion is captured using diffusion of the density while the rectified motion due to pheromone gradients is captured through chemotaxis, in addition to being self-propelled with a velocity  $\mathbf{u}_a$  that is related to the local environment. Finally, motivated by observations of antennation (**Gordon, 1999; Pagliara et al., 2018**), we assume that when the ants are stimulated by the presence of the corral past a threshold of antennation,  $c^*$  they start excavating. The rate of excavation is assumed to be proportional to the difference in the pheromone concentration relative to the threshold value i.e.  $\sim (c - c^*)$  (see SI sec. 1 further details). Accounting for these effects, we arrive at the following dynamical equations for the evolution of  $\rho_a(\mathbf{x}, t)$  and  $\rho_s(\mathbf{x}, t)$ :

$$\partial_t \rho_a = - \underbrace{\nabla \cdot (\mathbf{u}_a \rho_a)}_{\text{Self-propulsive advection}} + \nabla \cdot \left( \underbrace{D_a \nabla \rho_a}_{\text{Diffusive flux}} - \underbrace{\chi \rho_a \nabla c}_{\text{Tactile feedback}} \right), \quad (4)$$

$$\partial_t \rho_s = - k_s \rho_s \left\{ \underbrace{\Theta(c - c^*)}_{\text{Antennating field threshold}} \right\} \times \left\{ \underbrace{\Theta(\rho_a - \rho_a^*)}_{\text{Ant density threshold}} \right\}. \quad (5)$$

148 Here, in the first equation, the ant advection velocity is assumed to have the form  $\mathbf{u}_a = v_o(1 -$   
 149  $\rho_s/\rho_o)\hat{\mathbf{p}}$  where  $v_o$  is the characteristic speed of the agents, and  $\hat{\mathbf{p}}$  is a unit vector pointing along the  
 150 radial ( $\theta$ ) direction, and the term  $(1 - \rho_s/\rho_o)$  reflects the fact that excavating ants are slowed down  
 151 by their labor;  $D_a$  is the diffusivity of ants,  $\chi$  is a chemotactic gain associated with the strength of  
 152 antennating-field-following behavior that captures the intensity of the tactile feedback that ants  
 153 experience (related to the rotational  $G$  in the agen-based model);  $k_+$ ,  $k_-$  are the rate of production  
 154 and decay of the antennating/pheromone field, and  $D_c$  is its diffusivity (see SI sec. );  $k_s$  is the rate of  
 155 excavation of the corral and  $\rho_a^*$ ,  $c^*$  are the threshold concentration of ant density and antennating  
 156 field required to initiate excavation. We assume that the behavioral switches have simple switch-  
 157 like responses modeled here via the Heaviside function  $\Theta(x)$  (or its regularization via hyperbolic  
 158 or Hill functions). It is useful to note that in the absence of excavation dynamics, our framework  
 159 reduces to the well known Keller-Segel model for chemotaxis (see (**Hillen and Painter, 2009**) for  
 160 a recent review) (also detailed in SI sec. 2). The coupling of ant behavior to the dynamics of ex-  
 161 cavation introduces the all-important notion of *functional* collective behavior linking active agents,  
 162 communication channels (the antennating and pheromone fields) and a dynamic, erodible corral  
 163 that characterizes function in terms of progress towards task completion.

### 164 **Model parametrization and description**

The evolution of the ant density in **Equation 4** is a combination of three dynamical processes: ant migration, their diffusion and biased motion due to feedback from contact with other ants (captured using the antennating field). There are three time-scales associated with these three processes: ant density diffusion time-scale  $\tau_a \sim l^2/D_a$ , ant collective migration time-scale  $\tau_o \sim l/v_o$  and the time-scale associated with taxis due to antennating field gradient  $\tau_x \sim l^2/\chi c_o$ , where  $l$  is a characteristic length-scale which is either the width of the corral to be tunneled  $L$  (which is assumed to be of same order as width of initial ant density profile  $l_a$ ) or the length-scale due to antennating field diffusion and decay,  $l \sim (D_c/k_-)^{1/2}$  or the length-scale due to the advection of ant density and diffusion,  $l \sim D_a/v_o$ . The antennating field in **Equation 3** on the other hand is governed by three processes, which are the generation of antennating field at ant locations, decay and diffusion in the intensity representing loss in memory as well as errors in their measurements. We have three more time-scales due to these processes: antennating field production time-scale  $\tau_+ \sim c_o/(k_+ \rho_o)$ , diffusion time-scale  $\tau_c \sim l^2/D_c$ , and decay time-scale  $\tau_- \sim 1/k_-$ . Lastly, the corral is excavated as a

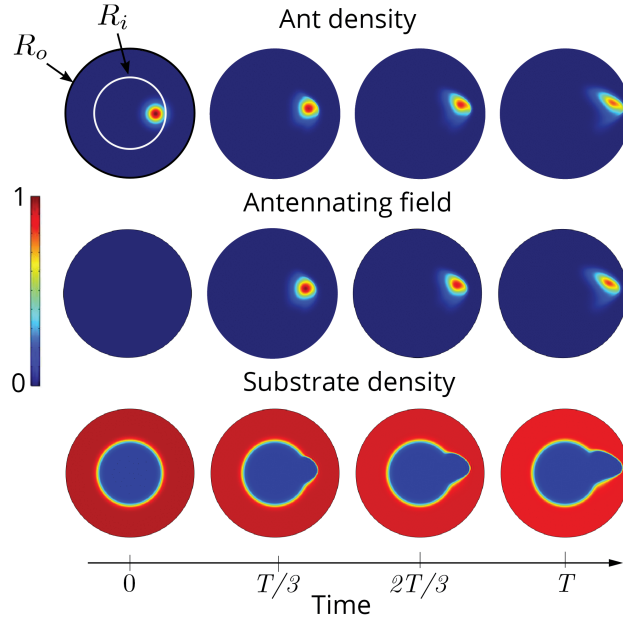


**Figure 5.** Two dimensional simulations showing the evolution of the ant density  $\rho_a$ , antennating field  $c$  and the corral density  $\rho_s$  by evolving **Equation 4-Equation 5**, capturing successful tunneling for non-dimensional numbers  $C = 0.8$ ,  $E = 1.44$  and time of simulation  $T = 20.0$ . The list of dimensional parameters used in the simulation are indicated in the SI **Figure 1(f)**. Radius of the outer boundary,  $R_o$  is 5 non-dimensional units and the inner boundary is  $R_i = 2.5$  (see SI 2 for details). Color bar shows the magnitude of different variables and they vary between 0-1.

function of time with a characteristic time-scale  $\tau_s \sim 1/k_s$  as in **Equation 5**. Here  $\rho_o$  is the average density of the ants defined by  $\rho_o = \int \rho_a dx / L$  where  $L$  is the domain size. This is a natural scale of the ant density as **Equation 4** is in conservative form and the net density of the ants is preserved over the evolution. The dynamics has the threshold  $c^*$  as the only intrinsic intensity scale of the antennating field. However this is not a natural scale for the antennating field as the threshold cannot be tuned but is often fixed in the system. Instead we use the maximum antennating field produced during the dynamics to be  $c_o$ . The list of time-scales and length-scales associated with the different processes in the model are in **Table 2**. With seven time-scales the parameter space of the model is quite large. We thus look at various limits in this parametric space to glean insights into the mechanisms of task execution. Although our model has a number of different time-scales parameters (see SI sec. 2 for a list along with their ranges), two non-dimensional numbers arising out of these different time-scales are qualitatively important in capturing the etho-space of collective excavation: (i) the scaled cooperation parameter defined as  $C = \tau_a / \tau_x = \chi c_o / D_a$  which determines the relative strength of antennation (gradient-following) to ant diffusion with  $c_o$  being the maximum amplitude of the antennating field, (ii) the scaled excavation rate,  $E = \tau_v / \tau_s = k_s l / v_o$ . Here,  $l / v_o$  is the characteristic time-scale of ant motion, with  $l \sim \min[(D_c / k_-)^{1/2}, l_a]$ , where  $l_a$  is the ant size (see SI sec. 2 for details). In addition, we have the ratio of ant motion time-scale vs the diffusive time-scale,  $V = \tau_x / \tau_a = v_o l / D_a$ . The three non-dimensional numbers  $C, E, V$  arise out of the dynamics of the ant density field in **Equation 4** and the corral in **Equation 5**. Two additional non-dimensional numbers follow from the dynamics of the antennating field in **Equation 3**: comparing the rate of production of pheromone with diffusion or decay, we write  $\hat{k}_{\pm} = \tau_- / \tau_{\pm} = k_{\pm} \rho_o / (k_- c_o)$  and  $D_c = \tau_- / \tau_c = D_c / (l^2 k_-)$ . Then the complete set of non-dimensional numbers that capture the dynamics of the ant collective is given by

$$C = \frac{\chi c_o}{D_a}, E = \frac{k_s l}{v_o}, V = \frac{v_o l}{D_a}, \hat{k}_{\pm} = \frac{k_{\pm} \rho_o}{k_- c_o}, D_c = \frac{D_c}{l^2 k_-}.$$

In terms of these parameters, the dynamics of the ant density, the antennating field and the corral density can be written in non-dimensional form as

$$\partial_t \rho_a + \nabla \cdot [(C\nabla c + V(1 - \rho_s))\rho_a] = \nabla^2 \rho_a, \quad (6)$$

$$\partial_t c = D_c \nabla^2 c + \hat{k}_\pm \rho_a - c, \quad (7)$$

$$\partial_t \rho_s = -\frac{1}{4} E \rho_s (1 + \tanh[\alpha_c (c - c^*)]) \times (1 + \tanh[\alpha_c (\rho_a - \rho_a^*)]). \quad (8)$$

165 To complete the formulation of our model, we also need to specify some initial conditions for the  
166 three fields and boundary conditions for the ant density, the pheromone density, and the location  
167 of the corral boundary which are detailed in the sec. 2.

## 168 Results

### 169 Linear analysis

170 Before we can look at the different limits of the phase-space defined by the non-dimensional num-  
171 bers, we show that the excavation process is an instability which is triggered by the scaled exca-  
172 vation parameter  $E$  in the system. We can see that the homogeneous state  $\rho_a^{SS} = \rho_a^*$ ,  $c^{SS} = c^* =$   
173  $k_+ \rho_o / k_-$ ,  $\rho_s^{SS} = 1$  is a steady state of the above equations. This steady state represents a special  
174 case where the density of the ants is close to the critical threshold and so is the strength of the  
175 antennating field. Perturbation analysis helps us determine the mode of instability close to this  
176 threshold where the ants have accumulated and generated an effective antennating field.

177 In order to understand the short time dynamics close to this steady state, we introduce a  
178 perturbation around this configuration and expand it using a plane wave ansatz. In 1D this be-  
179 comes:  $\{\rho_a(x, t) - \rho_a^{SS}, c(x, t) - c^{SS}, \rho_s(x, t) - \rho_s^{SS}\} = \{\tilde{\rho}_a(k), \tilde{c}(k), \tilde{\rho}_s(k)\} \exp(ikx + \Omega t)$  where we assume  
180 that  $\|\tilde{\rho}_a\|, \|\tilde{c}\|, \|\tilde{\rho}_s\| \ll 1$ . Then the linearized equations for ant density in **Equation 6** reads as:  
181  $(\Omega + k^2)\tilde{\rho}_a + ikV\tilde{\rho}_s\rho_o = k^2C\tilde{c}$  and the antennating field in **Equation 7** becomes:  $\tilde{c} = \hat{k}_\pm \tilde{\rho}_a / (\Omega + 1 + D_c k^2)$ ,  
182 and lastly the corral density in **Equation 8** becomes  $\Omega\tilde{\rho}_s = -E\tilde{\rho}_s/2$ . From this we see that the growth  
183 rate  $\Omega = -E/2$ , is independent of all other parameters in the system. Thus tunneling begins when  
184  $E > 0$ , once the ants have created a sufficiently large spatially diffuse antennating field, and the  
185 corral excavation rate determines the dynamics of the instability. To understand the dynamics of  
186 excavation of the corral and the different phases of collective behavior, we now explore the role  
187 of the other non-dimensional numbers.

### 188 Limits of phase-space

189 In this section we discuss the different limits of the phase-space defined by the non-dimensional  
190 numbers  $\{C, E, V, \hat{k}_\pm, D_c\}$  and the thresholds  $\rho_a^*, c^*$ . We use non-dimensional numbers to describe  
191 the region in phase-space but revert to dimensional form to keep the analysis mechanistically trans-  
192 parent.

193 Small thresholds, when  $\rho_a^* \ll \rho_o$  and  $c^* \ll c_o$

194 When  $\rho_a^* \ll \rho_o$  and  $c^* \ll c_o$ , partial tunneling can be achieved even if we start with an inhomogeneous  
195 ant density  $\rho_a$ , independent of the pheromone dynamics and is thus very inefficient. Depending on  
196 whether the ants can tunnel fast or slow relative to their motion, i.e. depending on the value of the  
197 ratio  $\tau_s/\tau_v$ , the ants can excavate through the corral completely ( $\tau_v/\tau_s \ll 1$ ) or partially ( $\tau_v/\tau_s \leq 1$ )  
198 (ref **Table 2**).

199 On the other hand if the ants are moving randomly, i.e. in the diffusion-dominated regime,  
200 then they can still tunnel through the corral if  $\tau_c \sim \tau_s$  and achieve partial tunneling if  $\tau_c \lesssim \tau_s$ . In non-  
201 dimensional terms this translates to  $V \sim \mathcal{O}(1)$ ,  $C \ll 1$  or  $V, C \ll 1$  for the ant density and  $E \sim \mathcal{O}(1)$  for  
202 the corral evolution. It is worth mentioning that we use the width of the corral,  $L$  as the relevant

203 length-scale to define these non-dimensional numbers. SI **Figure 1(a)** has simulations showing this  
 204 behavior both in the tunneling and the partial tunneling phase.

205 Cooperation dominated regimes when  $C \gg 1$  and  $E, V \rightarrow 0$

206 For efficient excavation, the ants need to work collectively, i.e. be localized and excavate fast. Lo-  
 207 calization in space leads to cooperation via feedback from the antennating field (see **Figure 4(b)**) -  
 208 this keeps the collective together and prevents it from diffusing away. For successful excavation,  
 209 ants also need to migrate towards the corral and tunnel through it, so that their effective speed  $v_o$   
 210 needs to be non-zero. We first look at the dynamics of the ant density and the antennating field in  
 211 the absence of migration i.e.  $V \rightarrow 0$  (we also neglect the corral dynamics for now). There are three  
 212 regimes arising out of the antennating field dynamics which we now consider separately:

- **Diffusion dominated regime:** When the generated antennating field rapidly diffuses away, i.e.  $D_c \sim \hat{k}_{\pm} \gg 1$ , then the antennating field and the ant density evolve as

$$-D_c \nabla^2 c = k_+ \rho_a, \quad (9)$$

$$\partial_t \rho_a + \chi \nabla \cdot (\rho_a \nabla c) = D_a \nabla^2 \rho_a. \quad (10)$$

213 In this limit, we obtain the well known Keller-Segel model for bacterial aggregation (**Hillen and**  
 214 **Painter, 2009**). Balancing the effects of diffusion of the antennating field with the production  
 215 term, we obtain a length-scale over which gradients in antennating field is felt which is  $l \sim$   
 216  $(D_c c_o / k_+ \rho_o)^{1/2}$ . Accumulation in ant density can happen when the ants can sense this gradient  
 217 which corresponds to large  $C$ . On the other hand for small  $C$ , the ant density diffuses out. The  
 218 diffusion of the antennating field drives migration of ants due to detection of gradients thus  
 219 resulting in generation of more antennating field in the new location. This process continues  
 220 to happen perpetually resulting in piling up of ant density.

- **Decay dominated regime:** When the generated antennating field all decays fast we are in the limit of  $\hat{k}_{\pm} \sim \mathcal{O}(1), D_c \ll 1$ . The dynamics of the antennating field reduces to  $c \approx (k_+ / k_-) \rho_a$ . The ant density evolution then becomes,

$$\partial_t \rho_a + \frac{\chi k_+}{k_-} \nabla \cdot (\rho_a \nabla \rho_a) = D_a \nabla^2 \rho_a. \quad (11)$$

221 When the chemocactic coefficient  $\chi$  is large, i.e. in dimensionless terms  $C \gg 1$ , the ant collec-  
 222 tive undergoes jamming. This can be seen most easily by linearizing the equation **Equation 11**  
 223 about a uniform ant density  $\rho_o$  and recognizing that this can lead to an effective negative dif-  
 224 fusivity and thus the onset of clustering and a spatio-temporal focusing of the ant density;  
 225 we leave a detailed analysis of the characteristics of this for future study.

- **Competing effects of diffusion and decay:** Comparing the diffusion of the antennating field and its decay, i.e. letting  $D_c \sim \mathcal{O}(1)$ , yields a length scale  $l \sim (D_c / k_-)^{1/2}$  which defines the zone of influence of the field. We use this length scale to arrive at the non-dimensional tunneling rate indicated in **Figure 8**. Then, in the limit when the antennating field generation rate is large, i.e.  $\hat{k}_{\pm} \gg 1$ , the field generates a gradient that drives collective ant motion and excavation.

232 All together, our analysis shows that the dynamics of the antennating field controls the aggregation  
 233 or diffusion of ant density. But this is alone is not enough; for efficient excavation, especially when  
 234 the activation thresholds for excavation and localization  $\rho_a^*, c^*$  are large, we need both cooperation  
 235 and finite velocity of migration so that the ant collective can eventually tunnel through. Other  
 236 regimes associated with partial tunneling, jamming or diffusion arise as the parameters are varied,  
 237 as listed in **Table 3**.

252 When accounting for the effects of excavation and migration of the ants i.e.  $E, V \neq 0$ , by solving  
 253 the governing **Equation 4-Equation 5** in a one-dimensional setting (ref SI sec. 2) captures the two  
 254 limits of the excavation behavior seen in experiments; For large excavation rate  $E$  and cooperation

239 **Box 1. Ant behavior → Model → Robot behavior**

240 Ants inside the corral move around, communicating with each other using their antennae  
 241 before they cooperatively excavate the agarose corral. Though the detailed spatio-temporal  
 242 dynamics of each ant's behavior is different at the microscopic level, we see that the coopera-  
 243 tion between the ants results in a persistent density front (see **Figure 1(d, e)** and **Figure 2**) that  
 244 excavates the substrate. In the theoretical description of the collective's dynamics, the relevant  
 245 behaviors are encoded through mutual interaction between the ants (via the antennating  
 246 field) and the substrate. Such a description also inspires the robotic mimics that capture the  
 247 ant collective's average behavior. We list below the comparison between relevant behaviors  
 248 in ants and their analogous encoding in the theoretical model as well as in the robots.

Ants	Theoretical model	Robots
Discrete ants	Ant density, $\rho_a(\mathbf{x}, t)$	Discrete robots
Antennae communication	Communication field, $c(\mathbf{x}, t)$	Photomone field
Agarose corral	Substrate density, $\rho_s(\mathbf{x}, t)$	Boundary elements
Motility	Self-propulsive advection, $\mathbf{u}_a$	Mobile agents
Exploratory behavior	Density diffusion, $D_a \nabla \rho_a$	Random walk
Tactile feedback	Antennating field taxis, $\chi \rho_a \nabla c$	Phototaxis
Biting behavior	Excavation rate, $k_s$	Collection and deposition
Neural control	Dynamics of ant density	Behavioral rules

250 **Box 1 Table 1.** Comparison of relevant variables, basic behaviors, and behavioral coordination between  
 251 ant experiments, theoretical model and robotic implementation.

255 parameter,  $C$ , we see coordinated excavation (shown in **Figure 4(b)**), while decreasing the cooper-  
 256 ation parameter leads to disorganized excavation (shown in **Figure 4(c)**) (see SI **Figure 1**). While  
 257 a direct comparison with the behavior of ants is not easy owing to the difficulty of inferring the  
 258 dynamics of information transfer through antennation, the minimal assumptions we have made  
 259 about the antennating field dynamics suffice to capture the macroscopic behavior of the collective.  
 260 All together, our agent-based model and the phase-field model shows the emergence of cooper-  
 261 ativity without the need for a plan, optimization principle, or an internal representations of the  
 262 world, but via the environmentally-mediated communication between agents (**Mataric, 1993**) that  
 263 leads to task completion.

264 **Robotic collective excavation**

265 Although the collective behavior of the ants is qualitatively captured by our simplified theoretical  
 266 model, we can ask if the coarse-grained averaging over microscopic dynamics of the communica-  
 267 tion field might affect the emergence of the task in experiments. It is thus unclear if the simplifying  
 268 assumptions underlying the model are sufficiently general, since we are unable to control the mi-  
 269 croscopic behaviors in the system. To go beyond our ability to merely explain the observations of  
 270 ant behavior using our theoretical framework, we asked if we might be able to synthesize or recre-  
 271 ate the behavior in robotic mimics, and probe a larger range of the parameters and phase-space  
 272 spanned by  $C, E$ , than our experiments allowed us to.

273 For this, we turn to a robotic platform to synthesize collective functional behaviors that arise  
 274 from simple behavioral rules underlying individual programmable robots. Our custom designed  
 275 robot ants (RAnts) are inspired by many earlier attempts to create artificial agents that are mobile  
 276 and follow simple rules (**Braitenberg, 1986; Brooks, 1991; Simon, 1996**), can respond to virtual  
 277 pheromone fields (**Sugawara et al., 2004; Garnier et al., 2007**) and are capable of robotic exca-  
 278 vation (**Aguilar et al., 2018**). Our autonomous wheeled robots can exhibit emergent embodied  
 279 behavior (**Bricard et al., 2013**), and are flexible enough to allow for a range of stigmergic interac-

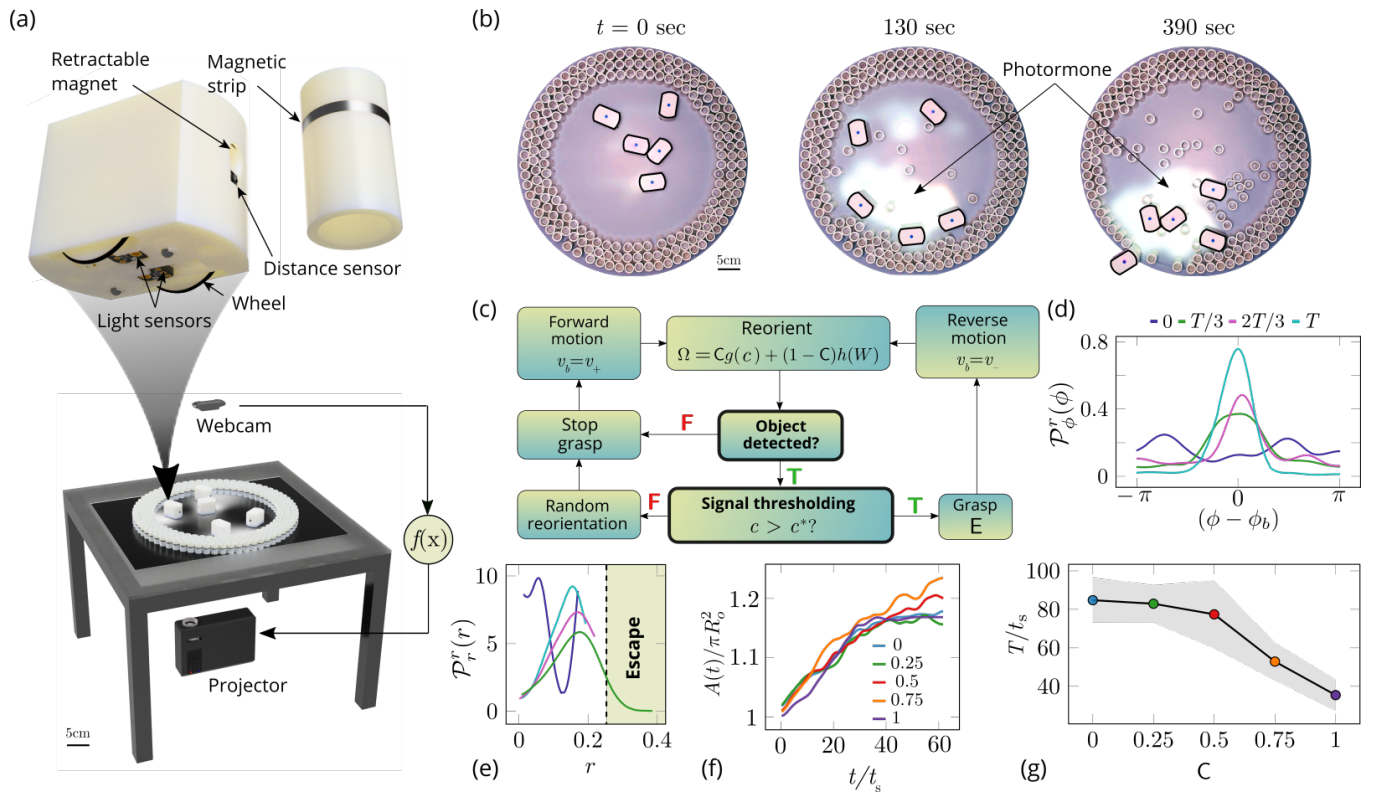


**Figure 6. Emergent cooperative excavation dynamics in robotic ants** (a) Robot Ant (RAnt) set-up. A mobile RAnt is placed in an arena 50cm in diameter surrounded by three layers of cylindrical boundary elements totalling 200 elements. The outermost layer is prevented from being pushed out of the arena by a circular ring. A scalar concentration field (*photormone* field) is projected onto a plane whose intensity can be measured by a RAnt. The position of each RAnt is tracked using a webcam. Each RAnt can pick up and drop the discrete boundary elements using a retractable magnet. (b) Series of snapshots at different times of the excavation process for a cooperation parameter  $C = 1$ . (c) Flowchart of the RAnt programming. A base locomotion speed  $v_b$  is stored internally and the rate of change  $\Omega$  of the heading is a function of the cooperation parameter  $C$ , the photormone concentration  $c$ , and a stochastic process  $W$  (Brownian motion). A photormone threshold  $c^*$  determines whether an object is grasped (with probability  $E$ ) after it is detected by the distance sensor. (d) Orientation distribution of the RAnt density  $\mathcal{P}_\phi^r(\phi, t)$  as a function of the azimuthal position  $\phi$ .  $\phi_b$  is the orientation of the excavated tunnel. The density is plotted for different times. (e) Radial distribution of the RAnt density  $\mathcal{P}_r^r(r, t)$  within a sector of  $\pi/2$  centered around the position of the excavated tunnel as a function of distance from the center of the arena  $r$ . The density is plotted for the same times as in (d). (f) Confinement area  $A(t)$  as a function of time, normalized by initial circular confinement with radius  $R_o$  for different cooperation parameter  $C$ . (g) Normalized excavation time  $T$  as a function of cooperation parameter  $C$ , averaged over 5 experiments per cooperation parameter. Every experiment was run until the first RAnt excavated out or the experiment duration exceeded 15 minutes.

280 tions with the environment (Werfel et al., 2014; Petersen et al., 2019). This is made possible by  
 281 having each RAnt equipped with an infrared distance sensor to detect obstacles and other RAnts,  
 282 a retractable magnet that can pick up and drop wall elements with a ferromagnetic ring (shown  
 283 in Figure 6(a)), and the ability to measure a virtual pheromone field generated by a light projected  
 284 (from below) onto the surface of a transparent arena they operate in (see Figure 6(a, b)) (Theraulaz  
 285 and Bonabeau, 1995; Sugawara et al., 2004; Garnier et al., 2007; Wang et al., 2021). The intensity  
 286 of this “photormone” field follows the antennating field Equation 3 and thus follows the dynam-  
 287 ics of a field that is linked to the the locations of the RAnts and diffuses and decays away from  
 288 it. The photormone field is realized by a projected luminous field on the arena, which the robots  
 289 can sense. This allows us to use a local form of Equation 4-Equation 5 to define a robot’s behavior  
 290 in terms of an excavation rate  $E$ , a cooperation parameter  $C$ , and a threshold concentration for  
 291 tunneling  $c^*$ . This is encoded in the behavior-based rules (see Figure 6(c) and SI sec. 3 for more  
 292 details), that induces the following behavior: (i) follow gradient of projected photormone field; (ii)  
 293 avoid obstacles and other RAnts at higher photormone locations; (iii) pick up obstacles from high  
 294 photormone locations and drop them at low concentration levels. Since the robots have no sym-  
 295 bolic representation of the different signals they sense (e.g. they cannot distinguish another RAnt

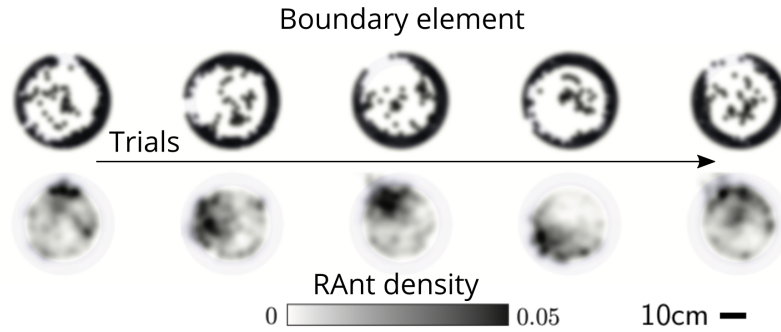


**Figure 7. Averaged RAnt dynamics** Ultimate distribution of boundary elements and averaged RAnt density field (in units of  $\#/cm^2$ ) over the full duration of experiments for different trials.

296 from a wall element, since both merely produce a bump in the sensor signal), the observed behav-  
 297 ior emerges from this simple sequence by depending on the current state of the environment and  
 298 the robot.

299 Varying the parameter  $C \in [0, 1]$  allows us to tune the individual behavior from random motion  
 300 ( $C = 0$ ) to tracking the photormone gradient ( $C = 1$ ). Varying the non-dimensional excavation rate  $E$   
 301 changes the frequency at which the robots execute pick-and-drop behavior with detected objects,  
 302 and serves to mimic what arises in ants as a function of their morphology and caste (see SI sec. 1 for  
 303 more details). For a specific value of these parameters, we followed the collective behavior of RAnts  
 304 by averaging their position over several pick-and-drop timescales to obtain the RAnt density field  
 305  $\rho_r(r, \phi, t)$ , just as for ants. When all the RAnts are programmed to have a cooperation parameter  $C =$   
 306 1, RAnts initially explore the region without picking the boundary element until the photormone  
 307 concentration  $c \sim c^*$ , which happens once a particular location has enough visits by other RAnts. As  
 308 for ants, we calculate the radially averaged RAnt density  $\mathcal{P}_r^r(\phi, t) = \int \rho_r(r, \phi, t) dr$ ; **Figure 6(d)** shows  
 309 how RAnt density localizes at a (random) value of the azimuthal angle. As excavation progresses,  
 310 the RAnt density propagates radially outwards as a density front just as in ants, shown in **Figure 6(e)**  
 311 in terms of the quantity  $\mathcal{P}_r^r(r, t) = \int \rho_r(r, \phi, t) d\phi$  (also shown in **Figure 7** for different trails when  
 312  $C = 1$ ). Concomitantly, as excavation progresses, the corral area increases (**Toffin et al., 2009**);  
 313 interestingly the scaled corral area  $A(t)/\pi R_0^2$  is independent of the cooperation parameter  $C$  as  
 314 shown in **Figure 6(f)** (all RAnts were programmed to have the same excavation rate).

315 However, cooperation does change the time for excavation; in **Figure 6(g)** we show the average  
 316 excavation time (scaled by the characteristic time it takes for a rant to traverse the arena) and  
 317 see that  $T/t_s$  decreases with an increase in the cooperation parameter  $C$ . RAnts excavated out  
 318 every time for  $C > 0.5$ , but are unable to complete excavation for low cooperation parameters  
 319 (within a 15 minute time window). Our results show that it is the localized collective excavation  
 320 of RAnts mediated by photormone-induced cooperation that is responsible for efficient tunneling  
 321 and excavation; for low values of the cooperation parameter, tunneling is defocused and global,  
 322 and thus not as effective (see SI **Figure 2**). When  $E \rightarrow 0$  (vanishing probability for a successful  
 323 pick up) but strong cooperation (see **Figure 8** and SI sec. for theoretical predictions), the RAnts get  
 324 jammed because they follow the photormone field they generate but are unable to tunnel through  
 325 the boundary constriction. On the other hand, when  $E$  is small and  $C$  is small, the agents do not  
 326 cooperate and their diffusive behavior prevents successful tunneling. The range of strategies can  
 327 be visualized in a two-dimensional phase space spanned by the variables  $E$  and  $C$  shown in **Figure 8**.  
 328 Low values of  $C$  and  $E$  lead to diffusive (and non-functional) behavior, while high values of these  
 329 variables lead to coordinated excavation, with the other two quadrants corresponding to jammed  
 330 states (large  $C$ , small  $E$ ) and partially tunneled states (large  $E$ , small  $C$ ). Interestingly, these states  
 331 are also observed as transients in our ant experiments, for example in the initially diffused state  
 332 that is characterized by random motion inside the corral, when transiently jammed states and

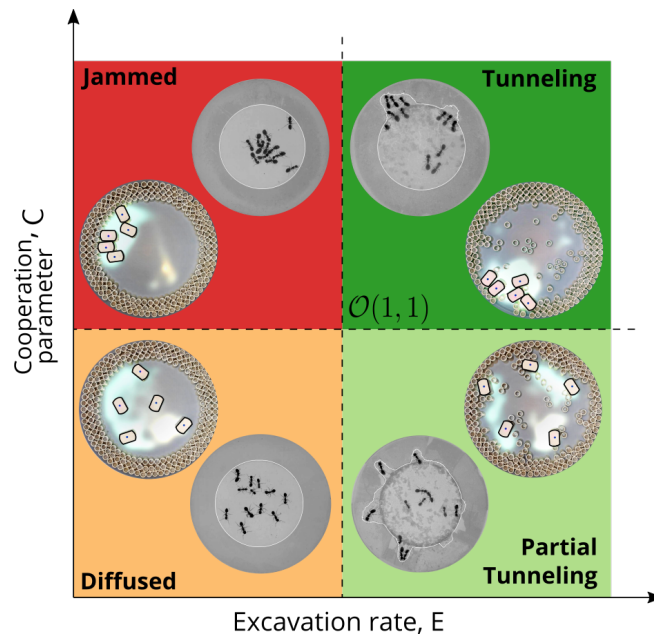


**Figure 8. Phases of cooperation** Phase-diagram of cooperative task execution with different phases seen in ants and RAnts. In the robotic experiments we tune the Cooperation parameter  $C$  and the Excavation rate  $E$  while in the ant experiments we change the caste mixture. In the ant experiments we see the jammed and diffused phases transiently before the ants relax to cooperative excavation.

333 partial tunneling occur (see Video3).

### 334 Discussion

335 Our analysis of collective behavior in a functional task, excavation, attempts to use observations  
 336 of ants to abstract the general features that are amenable to a theoretical treatment of the fields  
 337 and rules that are also sufficient to explain them, and eventually to create a robotic system that  
 338 recreates these behaviors. Simple dynamical models at the level of individual agents and an effec-  
 339 tive continuum theory explain our observations and provide a minimal phase diagram that shows  
 340 how the transition from an individually exploratory strategy to an exploitative cooperative solution  
 341 is mediated by the local chemical and mechanical environment. Our study suggested algorithms  
 342 that we then deployed in an engineered system of a swarm of robots that individually follow a min-  
 343 imal set of behavioral rules that mould the environment and are modulated by it. A critical aspect  
 344 of our framework is the role of a malleable environment that serves both as a spatial memory as  
 345 well as a computational platform (using the spatio-temporal photormone field and the corral). Our  
 346 simulations of agent-based models and robotic experiments further suggest that a coarse-grained  
 347 framework linking behavior, communication and a modulated environment is relatively robust to  
 348 failure of and stochasticity in the behavior of individual agents (i.e. variations in initial conditions  
 349 and number of agents), in the communication channels or in the corral geometry, in contrast to  
 350 many engineering approaches that aim to control all agents and optimize costs.

351 Different strategies such as collective excavation, jamming and diffusion then arise as a func-  
 352 tion of the relative strength of the cooperation (representing the ability to follow gradients and  
 353 detect threshold values) and excavation parameters (representing the ability to move material),  
 354 as manifest in a phase diagram, and the emergence of cooperation arises due to the relatively  
 355 slow decay of an environmental signal (the pheromone/antennating/photormone field), coupled  
 356 to a threshold excavation rate. Our approach to functional and purposeful collective behavior  
 357 links many simple brains and bodies with a dynamic environment that modulates behavior, and is  
 358 changed by it. Since the ability to solve complex eco-physiological problems such as collective exca-  
 359 vation is directly correlated with a selective advantage in an evolutionary setting, perhaps collective

360 behavior must always be studied in a functional context.

## 361 Acknowledgments

362 We thank the NSF PHY1606895 (S.G.P., L.M.), Swiss National Science foundation (F.G., grant P400P2-  
363 191115), Ford foundation (J.K.), NSF EFRI 18-30901 (L.M.), NSF 1764269 (L.M.), Kavli Institute for  
364 Bionano Science and Technology (S.M., V.M., L.M.), the Simons Foundation (L.M.) and the Henri  
365 Seydoux Fund (L.M.) for partial financial support.

## 366 References

- 367 **Aguilar J**, Monaenkova D, Linevich V, Savoie W, Dutta B, Kuan HS, Betterton M, Goodisman M, Goldman D.  
368 Collective clog control: Optimizing traffic flow in confined biological and robo-physical excavation. *Science*.  
369 2018; 361(6403):672–677.
- 370 **Alcock J**. *Animal behavior: An evolutionary approach*. Sinauer Associates Sunderland; 2001.
- 371 **Braitenberg V**. *Vehicles: Experiments in synthetic psychology*. MIT press; 1986.
- 372 **Bricard A**, Caussin JB, Desreumaux N, Dauchot O, Bartolo D. Emergence of macroscopic directed motion in  
373 populations of motile colloids. *Nature*. 2013; 503(7474):95–98.
- 374 **Brooks RA**. Intelligence without representation. *Artificial intelligence*. 1991; 47(1-3):139–159.
- 375 **Buhl J**, Deneubourg JL, Grimal A, Theraulaz G. Self-organized digging activity in ant colonies. *Behavioral ecology*  
376 and sociobiology. 2005; 58(1):9–17.
- 377 **Camazine S**, Deneubourg JL, Franks NR, Sneyd J, Theraulaz G, Bonabeau E. *Self-organization in biological sys-*  
378 *tems*. Princeton university press; 2020.
- 379 **Couzin ID**, Krause J, et al. Self-organization and collective behavior in vertebrates. *Advances in the Study of*  
380 *Behavior*. 2003; 32(1):10–1016.
- 381 **Deneubourg JL**, Franks NR. Collective control without explicit coding: the case of communal nest excavation.  
382 *Journal of insect behavior*. 1995; 8(4):417–432.
- 383 **Deneubourg JL**, Lioni A, Detrain C. Dynamics of aggregation and emergence of cooperation. *The Biological*  
384 *Bulletin*. 2002; 202(3):262–267.
- 385 **Elster J**, et al. *Social mechanisms: An analytical approach to social theory*. Cambridge University Press; 1998.
- 386 **Feinerman O**, Pinkoviezky I, Gelblum A, Fonio E, Gov NS. The physics of cooperative transport in groups of  
387 ants. *Nature Physics*. 2018; 14(7):683–693.
- 388 **Garnier S**, Tache F, Combe M, Grimal A, Theraulaz G. Alice in pheromone land: An experimental setup for the  
389 study of ant-like robots. In: *Swarm intelligence symposium IEEE*; 2007. .
- 390 **Gordon DM**. *Ants at work: how an insect society is organized*. Simon and Schuster; 1999.
- 391 **Gordon DM**. Movement, encounter rate, and collective behavior in ant colonies. *Annals of the Entomological*  
392 *Society of America*. 2021; 114(5):541–546.
- 393 **Gordon DM**, Paul RE, Thorpe K. What is the function of encounter patterns in ant colonies? *Animal Behaviour*.  
394 1993; 45(6):1083–1100.
- 395 **Hansen LD**, Klotz JH. *Carpenter ants of the United States and Canada*. Cornell University Press; 2005.
- 396 **Hillen T**, Painter KJ. A user's guide to PDE models for chemotaxis. *Journal of mathematical biology*. 2009;  
397 58(1):183–217.
- 398 **Hölldobler B**, Wilson EO, et al. *The ants*. Harvard University Press; 1990.
- 399 **Hölldobler B**, Wilson EO, et al. *The superorganism: the beauty, elegance, and strangeness of insect societies*.  
400 WW Norton & Company; 2009.
- 401 **Le Goc M**, Kim LH, Parsaei A, Fekete JD, Dragicevic P, Follmer S. Zooids: Building blocks for swarm user in-  
402 terfaces. In: *Proceedings of the 29th Annual Symposium on User Interface Software and Technology*; 2016. p.  
403 97–109.

- 404 **Mataric MJ.** Designing emergent behaviors: From local interactions to collective intelligence. In: *Proceedings*  
405 *of the Second International Conference on Simulation of Adaptive Behavior*; 1993. p. 432–441.
- 406 **Mikheyev A, Tschinkel W.** Nest architecture of the ant *Formica pallidefulva*: structure, costs and rules of  
407 excavation. *Insectes Sociaux*. 2004; 51(1):30–36.
- 408 **Nowak MA.** *Evolutionary dynamics: exploring the equations of life*. Harvard university press; 2006.
- 409 **Ocko SA, Mahadevan L.** Collective thermoregulation in bee clusters. *Journal of The Royal Society Interface*.  
410 2014; 11(91):20131033.
- 411 **Pagliara R, Gordon DM, Leonard NE.** Regulation of harvester ant foraging as a closed-loop excitable system.  
412 *PLoS computational biology*. 2018; 14(12):e1006200.
- 413 **Peleg O, Peters JM, Salcedo MK, Mahadevan L.** Collective mechanical adaptation of honeybee swarms. *Nature*  
414 *Physics*. 2018; 14(12):1193–1198.
- 415 **Pennisi E.** On the Origin of Cooperation. *Science*. 2009; 325(5945):1196–1199.
- 416 **Pereira TD, Tabris N, Li J, Ravindranath S, Papadoyannis ES, Wang ZY, Turner DM, McKenzie-Smith G, Kocher**  
417 **SD, Falkner AL, et al.** SLEAP: multi-animal pose tracking. *bioRxiv*. 2020; .
- 418 **Perna A, Theraulaz G.** When social behaviour is moulded in clay: on growth and form of social insect nests.  
419 *Journal of Experimental Biology*. 2017; 220(1):83–91.
- 420 **Petersen KH, Napp N, Stuart-Smith R, Rus D, Kovac M.** A review of collective robotic construction. *Science*  
421 *Robotics*. 2019; 4(28).
- 422 **Rahwan I, Cebrian M, Obradovich N, Bongard J, Bonnefon JF, Breazeal C, Crandall JW, Christakis NA, Couzin ID,**  
423 **Jackson MO, et al.** Machine behaviour. *Nature*. 2019; 568(7753):477–486.
- 424 **Rasse P, Deneubourg JL.** Dynamics of nest excavation and nest size regulation of *Lasius niger* (Hymenoptera:  
425 *Formicidae*). *Journal of Insect Behavior*. 2001; 14(4):433–449.
- 426 **Reinhard J, Srinivasan MV.** The role of scents in honey bee foraging and recruitment. Food exploitation by  
427 social insects: ecological, behavioral, and theoretical approaches. 2009; 1:165–182.
- 428 **Seeley TD.** *The wisdom of the hive: the social physiology of honey bee colonies*. Harvard University Press;  
429 2009.
- 430 **Simon HA.** *The sciences of the artificial*. 3 ed. MIT press; 1996.
- 431 **Sugawara K, Kazama T, Watanabe T.** Foraging behavior of interacting robots with virtual pheromone. In:  
432 *International Conference on Intelligent Robots and Systems*, vol. 3 IEEE; 2004. .
- 433 **Theraulaz G, Bonabeau E.** Coordination in distributed building. *Science*. 1995; 269(5224):686–688.
- 434 **Toffin E, Di Paolo D, Campo A, Detrain C, Deneubourg JL.** Shape transition during nest digging in ants. *Proceed-*  
435 *ings of the National Academy of Sciences*. 2009; 106(44):18616–18620.
- 436 **Trible W, Olivos-Cisneros L, McKenzie SK, Saragosti J, Chang NC, Matthews BJ, Oxley PR, Kronauer DJ.** Orco mu-  
437 tagenesis causes loss of antennal lobe glomeruli and impaired social behavior in ants. *Cell*. 2017; 170(4):727–  
438 735.
- 439 **Tschinkel WR.** The nest architecture of the Florida harvester ant, *Pogonomyrmex badius*. *Journal of Insect*  
440 *Science*. 2004; 4(1):21.
- 441 **Wang G, Phan TV, Li S, Wombacher M, Qu J, Peng Y, Chen G, Goldman DI, Levin SA, Austin RH, et al.** Emergent  
442 field-driven robot swarm states. *Physical review letters*. 2021; 126(10):108002.
- 443 **Waters CM, Bassler BL.** Quorum sensing: cell-to-cell communication in bacteria. *Annu Rev Cell Dev Biol*. 2005;  
444 21:319–346.
- 445 **Werfel J, Petersen K, Nagpal R.** Designing collective behavior in a termite-inspired robot construction team.  
446 *Science*. 2014; 343(6172):754–758.

## Videos

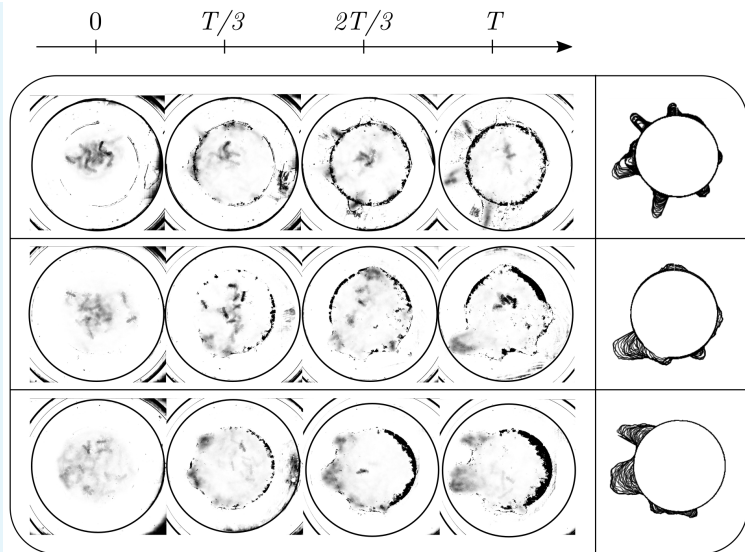
We have 4 supplementary videos which can be viewed using this [link](#).

1. Video 1 - Ant experiments: (i) Single ant: We confined 1 ant (major, media and minor individually) and capture their dynamics to see if they are capable of tunneling on their own; (ii) Multiple castes assemblage: We confined 12 ants, 4 for each of major, minor and media castes, and capture the dynamics of excavation as they tunnel through the boundary; (iii) Major ant collective excavation: We confined 12 major ants and capture the dynamics of excavation as they tunnel through the boundary.
2. Video 2 - Successful tunneling in RAnts: (i) Dynamics of excavation by RAnts as they cooperatively tunnel through the corral for  $C = 1$  and without cooperation,  $C = 0$ ; (ii) Jammed phase: When the pick-and-place in RAnts is deactivated (corresponding to  $E = 0$ ), they get jammed for  $C = 1$ ; Diffused phase: When the pick-and-place in RAnts is deactivated and the RAnts do not follow the antennating field (corresponding to  $C = 0$ ), they diffuse around.
3. Video 3 - Dynamics of excavation from agent-based simulation for different number of agents ( $n = 1, 5, 10, 22, 100$ ) in the corral for parameters in tab. 1. We see successful escape as well as trapped dynamics as highlighted in **Figure 3(d)**.
4. Video 4 - Summary video showing the results from ant experiments, theoretical model and robot experiments.

## Ant experiments

### Experimental setup - handling ants

We collected two queen-right mature colonies of *Camponotus pennsylvanicus*, established in logs of fallen trees, from the Middlesex Fells Reserve (42.45°N, 71.11°W) in August 2019. Each mature colony consists of three morphologically distinct castes of worker ants: major, media and minor, with an average body length of 7 mm, 5 mm for media, and 4 mm respectively. We placed the collected wooden logs housing those colonies in two separate plastic "home" boxes. We coated the inner wall of each home box with ant-slip Fluon to prevent the ants from escaping the home box. Each home box was connected to a foraging box by a tube through which ants travelled to and fro. We kept the whole set up in the laboratory with a 12 hour light-dark cycle, 30°C temperature and 50-70% relative humidity. Before we moved to the next phase of the experiment, i.e. the data collection, we waited for the ants to resume foraging and excavation of woods (for expanding their galleries) inside their home wooden log; this took 3-5 days after the relocation.



481  
482  
483  
485

**Appendix 1 Figure 1.** Dynamics of ant density field,  $\rho_a(x, t)$  (in units of  $\#/mm^2$ ) obtained by averaging the ant location and the boundary shape  $R(\phi)$  when 4 ants each of major, media and minor types are confined inside the agar ring for different trials.

486  
487  
488  
489  
490  
491

About 10 minutes prior to the experiments, we collected ants engaged in wood excavation from the surface of the nest log. We used insect aspirators for collecting the ants. Once we collected all ants needed for the experiment, we subjected the ants to Carbon dioxide anaesthesia for 1 minute. Next, we placed the anaesthetised ants in the agarose well in the experimental arena; we placed each ant at least 1 cm away from any other ant. Ants regained their activity in the next 5-10 minutes.

492

### Experimental setup - confinement

493  
494  
495  
496  
497  
498  
499  
500  
501  
502  
503  
504  
505  
506

For the next phase of the experiment, we needed to confine the ants in an excavatable enclosure. This is the corral that the ants need to bite through to free themselves. We used a ring-like confinement made of agarose gel, with a height of 10 mm, an inner radius of 35 mm and outer radius of 55 mm, making the ring 20 mm thick. To make a precise shape of the ring repeatedly, we custom-built a casting mold made of acrylic plastic. We started preparing for the Agar ring before we collected the ants. For making the ring, first, we thoroughly mixed 3 gm of Agar powder in 100 ml of tap water. We then warmed the solution in a microwave oven until the solution started bubbling and appeared clear. Next, we poured the solution in the plastic mold, and kept it in 30°C temperature for 25 minutes; the agarose gel solidified and become opaque during this time. Once the agarose turned solid, we placed the ring on top of plastic sheet in the arena. Next, we placed the ants inside the ring and put a petri dish lid on top of the agarose ring. Thus, we confined the ants - with a solid plastic floor and ceiling, and an excavatable agarose gel wall. A schematic of the set-up is shown in *Figure 1(b)*.

507

### Experimental setup - arena and video recording

508  
509  
510  
511  
512

The arena consists of a piece of white 3 mm thick plastic sheet as the substratum, illuminated with infrared back-light, and surrounded by a 1.5 cm high plastic wall coated with Fluon ant-slip. We placed a Point Grey (FLIR) Grasshopper3 GS3-U3-41C6NIR camera, fitted with a 65 mm macro lens, on top of the arena to capture the view of the whole ring. The camera recorded the videos with 30 fps recording speed and 1024x1024 pixels resolution.

513  
514  
515  
516  
517  
518  
519  
520  
521  
522  
523  
524  
525  
526  
527  
528  
529  
  
530  
531  
532  
533  
534  
535  
536  
537  
538  
539  
540  
541  
542  
  
543  
544  
545  
546  
547  
548  
549

### Markerless tracking

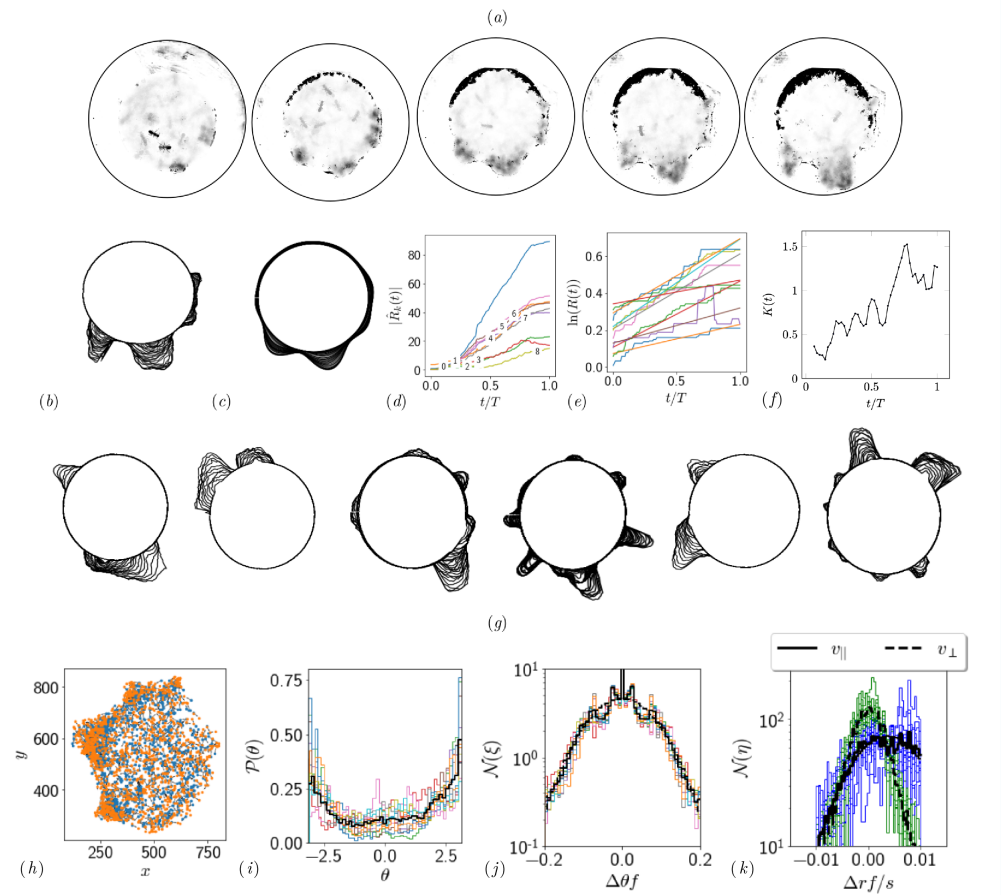
Leveraging an open source, deep-learning based pose estimator package SLEAP (*Pereira et al., 2020*), we track 3 body parts in each ant - head, thorax, and abdomen (gaster). Sample results obtained from this tracking is shown in SI *Figure 2(e)* and in *(f - h)* we quantify the noise statistics of ant motion and its orientation using the tracking data. Ants initially move randomly in the confinement and one of the ants starts the excavation process after which several ants start excavating cooperatively at the same location. When the tunneling happens, all the ants are orientated along the tunnel. We see this through the progression of the orientation distribution of ants  $\mathcal{P}(\theta, t)$  in SI *Figure 2(j)*. To characterize the localization in ant orientation as the excavation proceeds, we use a von-Mises distribution (the analog of a Gaussian distribution for a periodic variable, given by  $\mathcal{P}(\theta, t; \mu(t), K(t)) = \exp[K \cos(\theta - \mu)] / 2\pi I_0(K)$ ) of the ants (where  $\mu$  is the mean local orientation associated with location of tunnel along the boundary). In SI *Figure 2(k)*, we see that over time,  $K(t)$  increases, i.e. the variance decreases. During the excavation process, ants bite through the corral, carry the debris from the excavation site and drop it in the interior of the confinement. This happens over and over again until all the ants excavate out. We see this captured in the oscillations of the location of ants as shown in SI *Figure 2(i)*.

### Average dynamics

We have a total of 7 sets of experiments with four sets of experiments with a collective of 12 majors ants and 3 sets of experiments with a mixture of 4 major, 4 media and 4 minor ants. Using the recorded video of the ant excavation dynamics, we threshold the intensity to extract only the ant boundary and average the ant dynamics over 250 secs. This gives us a density field of ants representing the locations where the ants have been and the amount of time they spend. We found in our experiments that each ant bites the corral, picks the bitten piece and transports it into the interior of the confinement. This process takes approximately 60 secs (see SI *Figure 2(i)*) and we would like to average the ant dynamics over several 'turn over' time-scales. We chose 250 secs and the obtained density field is shown in SI *Figure 2*. We perform this averaging for the experiments with all major ants as well as the mixture of different castes. In all the experiments, an ant density front propagates through the corral as they excavate and gradually tunnel through.

### Boundary tracking

From the recorded videos, we also track the locations in which the ants excavate for creating the tunnel. For that, we used a custom image processing Matlab script. First, we created a mask superimposing on the area encircled by the inner ring of the corral; we colored the mask with a shade different from the corral. When ants excavated the corral, the Matlab script could detect the difference in the shade/color of the excavated area. Using this contrast, we track the continuously changing boundary.



550

551

552

553

554

555

556

557

558

559

560

561

562

563

564

565

566

567

568

569

570

**Appendix 1 Figure 2.** (a, b) Shape of the boundary tunnel during the tunneling process and the approximate representation of the shape using first 9 Fourier modes. (c) Evolution of the magnitude of the first 9 Fourier modes of the boundary:  $R(\phi, t) = \sum_k \hat{R}(k, t) e^{ik\phi}$ . (d) Evolution of boundary location,  $R(t)$  at different  $\phi$  values and the excavation rate. (e) Collage of boundary evolution showing tunnel formation in six experiments. (f)  $K(t)$  is the von Mises parameter highlighting strength of focus in ant orientation thorough a fit to the  $\mathcal{P}(\theta)$  obtained by a curve fit to the distribution. (g) Image showing evolution of the boundary as the excavation process happens for different experimental trials. (h) Location of center of ants with orientation during the excavation process. (i) Average orientation distribution  $\mathcal{P}(\theta)$  of all the ants showing hints of localization which is evident when plotted over time. (j) Noise statistics of ant velocity along the body axis,  $v_{\parallel}$  and in the normal direction,  $v_{\perp}$ . Dashed lines again are Gaussian fit to the data. Ants have zero mean velocity normal to its axis. (k) Noise statistics of orientation with peak close to 0 because of resting of the ants which otherwise follows a Gaussian which is the dashed line.

This is shown as a super-imposed image on the right side of SI **Figure 2** where  $R(\phi, t)$  is the radius of the ring as a function of the polar angle  $\phi$ . Tunnels are locations along  $\phi$  which see increase in the radius. We quantify this by plotting  $R(t)$  in SI **Figure 2**(d). We also quantify the number of tunnels by decomposing the shape into different Fourier modes as detailed in the caption.

### Agent-based model of cooperative task execution

The results shown in figure 3 are based on a numerical simulation where discrete agents operate in a continuum scalar communication field, subject to Equation (1) - (3). Some additional behavioral rules have to be defined to model the interaction of agents with the substrate. We realize the substrate by discrete obstacles arranged in a circular ring. Agents will attach to an obstacle if they are within the detection range,  $l_d$ , and if the measured communication field value is above the threshold, i.e.  $c \geq c_{hi}^*$ . The agent will then reverse its direction of motion, by changing the sign of  $G$  in Equation (2). This results in a gradient descent behavior and the attached obstacle will be detached once the measured communication field value satisfies  $c < c_{lo}^*$ . After detachment, the sign of  $G$  is changed again. If agents encounter other agents or obstacles within the detection radius but  $c < c^*$ , the agents will avoid the obstacle by turning randomly.

There are a few tuned behaviors we implemented to allow scaling the simulation to larger numbers of agents while maintaining the tunneling behavior. First, the gradient  $\nabla_{\perp} c$  in Equation (2) is passed through a  $\tanh(\cdot)$  function to limit the turning rate of the agents. Second, the noise term in Equation (2) was set to zero for this simulation and the only source of randomness are the random turns during obstacle avoidance. Third, agents pause for  $t_{p1}$  when they encounter an obstacle and for  $t_{p2}$  when picking up an obstacle. This helps disrupting potential "pheromone traps" to be formed where agents are bound to a region of space due to a high field concentration.

The simulation parameters are described in the following table. All parameters are non-dimensionalized by the corral size  $L$  and the base speed of the agents,  $v_0$ .

Parameter	Description	Value
$n_r$	Number of agents	1-100
$n_o$	Number of substrate elements	300
$n_l$	Number of corral layers	3
$T$	Maximum simulation time	66
$k_+$	Communication field production rate	97.5
$k_-$	Communication field decay rate	0.75
$D_a$	Communication field diffusivity	$4.2 \times 10^{-3}$
$c_{hi}^*$	Excavation threshold	$\frac{1}{2} \frac{k_+}{k_-}$
$c_{lo}^*$	Detachment threshold	0.11
$\sigma_g^2$	Agent field production width (variance)	$2.8 \times 10^{-3}$
$l_d$	Agent obstacle detection range	0.03
$t_{p1}$	Pause after obstacle detection	0.07
$l_{p2}$	Pause after substrate attachment	0.27
$G$	Rotational gain	0.135

Appendix 2 Table 1. Parameters of agent-based simulation.

597

## Continuum model of cooperative task execution

The dimensional equations for the ant-density  $\rho_a(\mathbf{x}, t)$ , antennating field  $c(\mathbf{x}, t)$  and the corral  $\rho_s(\mathbf{x}, t)$  are given by,

$$\partial_t \rho_a + \nabla \cdot (\mathbf{u}_a \rho_a) = \nabla \cdot (D_a \nabla \rho_a - \chi \rho_a \nabla c), \quad (12)$$

598

$$\partial_t c = D_c \nabla^2 c + k_+ \rho_a - k_- c, \quad (13)$$

599

600

$$\partial_t \rho_s = -\frac{1}{4} k_s \rho_s (1 + \tanh[\alpha_c (c - c^*)])$$

601

$$(1 + \tanh[\alpha_c (\rho_a - \rho_a^*)]), \quad (14)$$

602

603

604

605

606

607

608

609

where velocity of the collective is  $\mathbf{u}_a = v_o(1 - \rho_s/\rho_o)\hat{\mathbf{p}}$ , capturing the reduction in velocity as the ant collides with the corral. We approximate the Heaviside function,  $\Theta(x)$  here using the hyperbolic function  $[1 + \tanh(x)]/2$ . In the coarse-grained picture describing the collective tunneling seen in experiments the relevant variables (shown schematically in **Figure 4**) are the density of ants,  $\rho_a$ ; their velocity,  $\mathbf{u}_a$ ; amplitude of the antennating field,  $c$ ; the density of corral,  $\rho_s$ . Here we discuss the limits of phase-space that are not described in the main text i.e. when  $E \neq 0$  and also the simulation details.

Time-scale	Process
$\tau_a \sim l^2/D_a$	Ant diffusion
$\tau_v \sim l/v_o$	Ant collective migration
$\tau_x \sim l^2/(\chi c_o)$	Taxis due to antennating field gradient
$\tau_+ \sim c_o/(k_+ \rho_o)$	Antennating field production
$\tau_c \sim l^2/D_c$	Antennation field diffusion
$\tau_- \sim 1/k_-$	Antennating field decay
$\tau_s \sim 1/k_s$	Corral excavation
Length-scale	Process
$L$	Corral width
$l_a$	Initial width of ant density
$D_a/v_o$	Ant density advection-diffusion
$(D_c/k_-)^{1/2}$	Antennating field diffusion-decay

611

612

**Appendix 2 Table 2.** Time-scales and length-scales associated with different processes in the model in **Equation 12- Equation 14**.

614

615

616

617

618

619

620

621

622

623

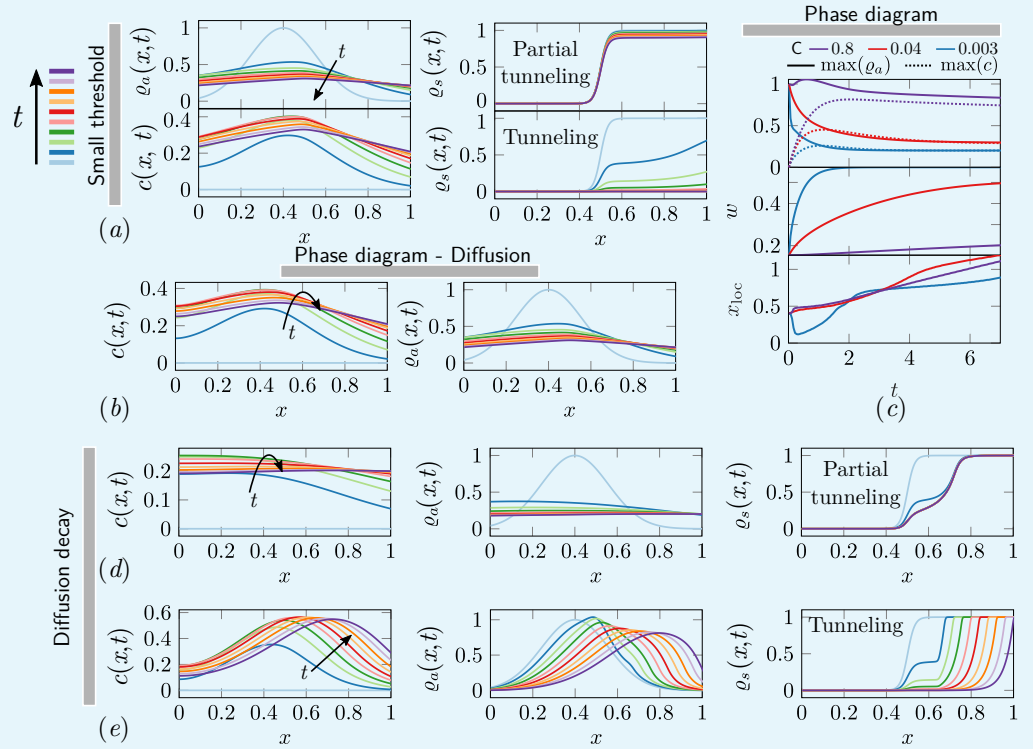
### Limits of phase-space when $E \neq 0$

Different phases of task execution/failure arise when the excavation parameter  $E$  and the cooperation parameter  $C$  are varied. In the cooperation dominated phase if the excavation rate of the agents is small, they get jammed and the analysis in the previous section holds true. When the cooperation among the agents is low, we have  $C \ll 1$  which results in diffusion dominated regime. Based on the strength of the excavation parameter  $E$ , the corral can be partially tunneled or just diffuse. Since we assume that the relevant length scale is of the same order as the width of the corral,  $L \sim l$ , our analysis reduces to different phases based on whether  $E \gg 1$  (where we get partial-tunneling) or  $E \ll 1$  (we get diffusion). Based on this we get partial tunneling or diffused phase as listed in **Table 3**.

In **Figure 1** we show results from 1-D simulations highlighting the effect of different terms we have discussed from **Equation 4-Equation 5** corresponding to different parts of the phase space of cooperative excavation. In the ant density diffusion dominated regime, i.e.  $C \ll 1, E \ll 1$ , shown in **Figure 1(b)**, there is little cooperation; rapid diffusion with slow excavation results in no tunneling. As we have seen in **Figure 4(b, c)**, tunneling and partial tunneling are inferred through the ultimate state of the corral and the ant-density. In

626  
627  
628  
629  
630  
631  
632  
633  
634  
635  
636  
637  
638  
639

SI **Figure 1(d, e)** we show how the relative rate of the antennating field diffusion compared to decay, i.e.  $D_c \sim \mathcal{O}(1)$  leads to either tunneling or partial tunneling as we vary the cooperation parameter  $C$ . Decreasing  $C$  causes the maximum of  $\rho_a(x, t)$ ,  $c(x, t)$  to go down (ref SI **Figure 1(c)**), and the width of the initial ant density field increases. Increasing  $C$  leads to successful tunneling driven by the propagation of the location of maximum ant density  $x_{loc}$  due to excavation of the corral. Furthermore, we see that the ants can be jammed either because the antennating field diffusion dominates, i.e.  $D_c \sim \hat{k}_{\pm} \gg 1$ , or because of the same field decays rapidly, i.e.  $\hat{k}_{\pm} \sim \mathcal{O}(1)$ ,  $D_c \ll 1$ . In both these cases however cooperation is what drives the aggregation. Lastly, we see that in order to achieve partial tunneling there are several routes depending upon the relative magnitudes of  $\{C, E, V, \hat{k}_{\pm}, D_c\}$  listed in **Table 3**.



	Phase	$v_o$	$\chi$	$D_a$	$k_+$	$k_-$	$D_c$	$k_s$
Small threshold	Tunneling	0.1	0	0.1	-	-	-	2.5
	Partial-tunneling	0.1	0	0.1	-	-	-	0.03
Phase diagram	Tunneling	0.1	$5 \times 10^{-3}$	$5 \times 10^{-3}$	1.5	1.5	$5 \times 10^{-3}$	2.5
	Partial-tunneling	0.1	$5 \times 10^{-3}$	$5 \times 10^{-1}$	1.5	1.5	$5 \times 10^{-3}$	2.5
	Partial-tunneling II	0.1	$5 \times 10^{-3}$	$5 \times 10^{-2}$	1.5	1.5	$5 \times 10^{-3}$	2.5
	Diffusion	0.1	$5 \times 10^{-3}$	0.1	1.5	1.5	$5 \times 10^{-3}$	0.001
Diffusion decay	Tunneling	0.1	$5 \times 10^{-3}$	$5 \times 10^{-3}$	1.5	1.5	$5 \times 10^{-2}$	2.5
	Partial-tunneling	0.1	$5 \times 10^{-3}$	$5 \times 10^{-1}$	1.5	1.5	$5 \times 10^{-2}$	2.5
(f) 2D	Tunneling	0.1	$5 \times 10^{-3}$	$5 \times 10^{-3}$	1.5	1.5	$5 \times 10^{-3}$	1.0

**Appendix 2 Figure 1.** The ant density field  $\rho_a(x, t)$ , antennating field  $c(x, t)$  and corral density  $\rho_s(x, t)$  for various scenarios of interest in the phase-space: (a) partial tunneling and tunneling when the threshold for excavation is small i.e.  $\rho_a^* = c^* = 0.01$ , we see homogeneous excavation and can get tunneling and partial tunneling; (b) when we are in the diffusive phase where ant density diffusion dominates,  $C = 0.02$  and the excavation rate is very small,  $E = 6 \times 10^{-4}$ ; (d, e) partial tunneling and tunneling when the length scale due to antennating field diffusion and decay is of the same order as the initial ant density i.e.  $l_a \sim (D_a/k_-)^{1/2}$ . (c) Evolution of maximum value of  $\rho_a, c$  for 3 different  $C$  and fixed  $E = 1.44$ . (f) Table with parameters used in simulations corresponding to different titles shown in gray bar in (a – e).

640  
641  
642  
643  
644  
645  
646  
647  
648  
649  
650

651

C	E	V	$\hat{k}_{\pm}$	$D_c$	Phase
$\gg 1$	$\gg 1$	$\gg 1$	$\mathcal{O}(1)$	$\ll 1$	Tunneling
$\gg 1$	$\gg 1$	$\gg 1$	$\ll 1$	$\mathcal{O}(1)$	Tunneling
$\ll 1$	$\gg 1$	$\gg 1$	$\mathcal{O}(1)$	$\ll 1$	Partial-Tunneling
$\ll 1$	$\gg 1$	$\gg 1$	$\ll 1$	$\mathcal{O}(1)$	Partial-Tunneling
$\gg 1$	$\ll 1$	-	$\mathcal{O}(1)$	$\ll 1$	Jammed
$\gg 1$	$\ll 1$	-	$\ll 1$	$\mathcal{O}(1)$	Jammed
$\ll 1$	$\ll 1$	-	-	-	Diffused

653

**Appendix 2 Table 3.** Different phases in different limits of phase-space of parameters in the model.

654

### Simulation details

655

656

657

658

659

660

661

662

663

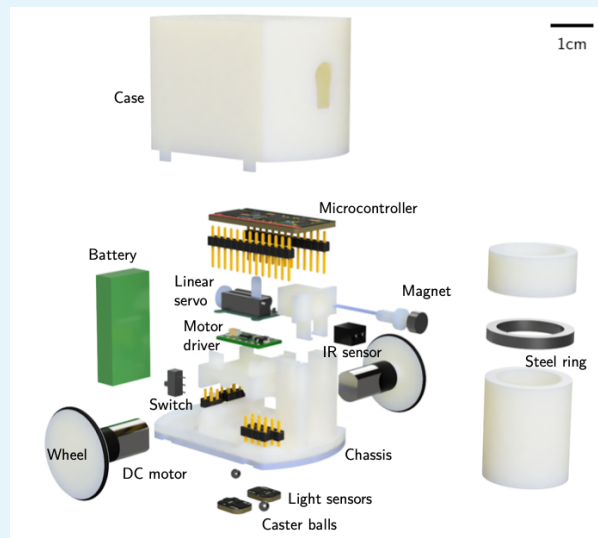
664

665

All the simulations shown in the main text as well the ones above were performed using commercial software COMSOL<sup>TM</sup>, in their general form Partial Differential Equations solver. We choose a very fine resolution with maximum mesh size of 0.005 in a domain of size 2 units in 1D simulations and maximum mesh size of 0.25 in a circular domain of radius 5 units in 2D. The initial condition for the ant density,  $\rho_a(r, 0)$  is  $\exp(-(r - r_o)^2/2l_a^2)$  where  $r_o = 0.4$ ,  $l_a = 0.16$  and the density of the corral  $\rho_s(r, 0)$  is chosen to be  $[1 + \tanh(\alpha(r - 2.5))]/2$  where  $\alpha = 30$ . We set the parameter  $\alpha_c = 50$  in 1D,  $\alpha_c = 10$  in 2D while  $\rho^* = 0.3$ ,  $c^* = 0.01$ . The other parameters used in the simulations in **Figure 4**, **SI Figure 1** and **Figure 5(a - e)** are listed in **(f)**. In the 2D simulations in **Figure 5** we assume a spatio-temporally varying self-propulsive velocity field of the form,  $\mathbf{u}_a = v_o \{\exp(-y^2/2\sigma^2), \exp(-t/\tau)(1 - \exp(-(x - x_o)^2/2\sigma^2))\}$ ,  $v_o = 0.1$ ,  $x_o = 0.2$ ,  $\sigma^2 = 0.75$ ,  $\tau = 10$ .

667 **Robot Ants**668 **RAnt design**

669 RAnts were designed to accommodate the essential electronic and electromechanical parts  
 670 required for locomotion, picking and placing, and sensing. An exploded view is shown in  
 671 **Figure 1**. RAnts are powered with a rechargeable 3.7V battery with 400mAh (Pkcell LIPO  
 672 801735) and are coordinated with a microcontroller (Adafruit ItsyBitsy M0 Express). The  
 673 RAnt's wheels have a diameter of 25mm and are directly driven with two brushed DC motors  
 674 with a planetary gearbox rated at 85 RPM at 3.7V. Rubber o-rings are attached to the wheels  
 675 to increase traction. A dual motor controller (Pololu DRV8835 Dual Motor Driver Carrier)  
 676 sets the desired output speed of the motors given a PWM signal from the microcontroller.  
 677 The mechanism to pick up wall elements was realized using a permanent magnet that is re-  
 678 tractable inside the RAnt. A linear servo motor (Spektrum SPMSA2005) moves a permanent  
 679 magnet inside a guide such that, when fully extended, the magnet attracts ferromagnetic  
 680 materials and when retracted, the magnetic force is small enough to drop any previously at-  
 681 tached  
 682 objects.  
 683  
 684  
 685  
 686



669 **Appendix 3 Figure 1.** Exploded view of a RAnt and a wall  
 670 element.  
 671  
 672  
 673

The objects to be picked up  
 are cylindrical wall elements of  
 dimension 22mm×40mm made  
 of polyvinyl chloride (PVC) tubes  
 which have a ferromagnetic ring  
 of 3mm thickness embedded in  
 them. The ring was 3D printed  
 using polylactic acid (PLA) mixed  
 with steel powder (colorFabb  
 SteelFill) and was sandwiched  
 between two PVC tubes. If the  
 RAnt is sufficiently close ( $\approx 3$ mm)  
 to a wall element with an en-  
 gaged magnet, the ring in the  
 wall element is attracted to the  
 magnet and the wall element is  
 slightly lifted from the ground  
 ( $\approx 1$ mm) for transportation due  
 to the elevated position of the  
 magnet relative to the ferro-  
 magnetic ring. RAnts have two

typers of sensors; two light sensors (Adafruit ALS-PT19) located at the bottom left and right of the RAnt (relative to the direction of travel) and an infrared (IR) distance sensor (Everlight ITR20001 opto interrupter) capable of detecting objects within 3cm in front of the RAnt. The chassis of the RAnt is 3D printed using acrylic styrene acrylonitrile (ASA) and supports all the internal components. The wheels of the RAnts were printed with the same material. Due to the design of the wheel arrangement, which was inspired by the zoid robots (**Le Goc et al., 2016**), we require two small steel caster balls of 3mm in diameter that help stabilize the RAnt. The steel balls can be pressed into the bottom of the 3D printed chassis. A 3D printed case made of ASA encloses all internal components of the RAnts, except for a small switch to power the RAnt on or off. A small blue sticker of 6mm in diameter was placed on the center top of the case and is used for tracking of the RAnt's position with the webcam

715  
716  
717  
718  
719  
720  
721  
722  
723  
724  
725  
726  
727  
728  
729  
730  
731  
732  
733  
734  
735  
736  
737  
738  
739  
740  
741  
742  
743  
744  
745  
746  
747  
748  
749  
750  
751  
752  
753  
754  
755  
756  
757  
758  
759  
760  
761  
762  
763  
764  
765  
766

mounted above the arena.

### RAnt programming

The RAnt behavior is coordinated by the microcontroller which we programmed according to the pseudocode shown in Algorithm 1. The program is initialized with a variable  $d$  that encodes the direction of travel (1 for forward, -1 for backward), the cooperation parameter  $C \in [0, 1]$ , the RAnt's base speed  $v_b$ , and the light intensity threshold  $c^*$ . This threshold was set at 50% of the maximal light intensity that can be generated by the photormone field multiplied by the cooperation parameter, i.e.  $c^* = 0.5 \times c_{max} \times C$ .

After initialization, the program enters a while loop which is running until the RAnt is switched off or the battery voltage drops below 3.5V. The loop starts with setting the heading of the RAnt, which effectively sets the turning rate. The turning rate is a function of the cooperation parameter and a stochastic process  $W$  (Wiener process) which is integrated in the microprocessor. The turning rate follows the equation

$$\Omega = Cd \frac{c_L - c_R}{c_{max}} + (1 - C) b \sin(\pi W) \quad (15)$$

with  $c_L$  and  $c_R$  the photormone intensity measured in the left and right light sensors, respectively,  $c_{max}$  is the maximal photormone intensity measurable by the sensors, and  $b = 0.3$  is a fixed amplitude. Using a sine function we map the stochastic process  $W$  to the range  $[-1, 1]$  to avoid getting stuck in constant rotation for large excursions of  $W$ . The first term in **Equation 15** corresponds to phototaxis using the projected photormone and the second term to a random walk. We can tune the influence of either terms with the cooperation parameter  $C$  from pure phototaxis at  $C = 1$  to a random walk at  $C = 0$ . The turning rate is used to define the rotation speed of each wheel. One wheel is always turning at a base rate  $\omega_1 = \omega_b = v_b/R$  (with  $R$  the wheel's radius) and the other wheel at

$$\omega_2 = \omega_b (1 - 2\|\Omega\|). \quad (16)$$

The assignment of  $\omega_1$  and  $\omega_2$  to the left and right wheel is flipped according to the sign of  $\Omega$ . With this definition, at a value of  $\Omega = \pm 1$  a RAnt turns on the spot without any translation and at  $\Omega = 0$  the RAnt moves on a straight path without rotation.

After the heading was defined and the turning rates sent to the motor driver, the distance sensor is checked for any obstacles that are present up to 3cm in front of the RAnt. At the same time, the light sensors are checked and compared to the threshold value  $c^*$ . If an object is detected and the photormone value exceeds  $c^*$ , the RAnt performs a fetching manoeuvre that consists of engaging the magnet with probability  $E$ , moving forward for a second with half the base speed  $v_b$  then move backwards for the same amount of time. After the fetching manoeuvre, the direction parameter is inverted, i.e.  $d = -1$ . If an object is picked up with the magnet after the fetching manoeuvre, the distance sensor will report a detected object as long as it is attached to the magnet. Since  $d = -1$ , the RAnt will perform the same type of gradient driven locomotion described in **Equation 15** and **Equation 16** but the sign of the signal sent to the motor driver will be inverted, resulting in a reverse motion of the RAnt. If an object is detected, but the photormone concentration in both sensors is lower than  $c^*$ , an avoidance manoeuvre is performed which consists of a random rotation in place in any direction with the intent to turn away from the detected obstacle.

The next if-statement checks again if an obstacle is detected, but without the condition that the direction parameter is equal to one. If no obstacle is detected, the direction parameter  $d$  is set to one and the magnet is disengaged.

---

**Algorithm 1:** RAnt behavioral algorithm

---

**Result:** Cooperative escape in Robot Ants

```
d = 1;
C ∈ [0, 1];
c* = 0.5 × cmax × C;
while true do
  set heading;
  if object detected & d = 1 then
    if c > c* then
      engage magnet with probability E;
      fetch object;
      d = −1;
    else
      turn away from object;
    end
  end
  if no object detected then
    d = 1;
    disengage magnet;
  end
  if d = −1 and P < kC then
    disengage magnet;
    turn away from object;
    d = 1;
  end
end
```

---

767

768

769

770

771

772

773

774

775

776

This guarantees that if a fetching manoeuvre is performed but the wall element was not picked up or the object was another RAnt, the RAnt goes back to moving forward.

The last if-statement checks whether the RAnt is in the reverse mode  $d = -1$  and if the photormone concentration dropped below the threshold  $c^*$ . If both statements are true, the magnet is disengaged, dropping any potentially picked up wall elements, and the direction parameter is set back to  $d = 1$ . In order to avoid the RAnt from picking up the just dropped element, it performs a random rotation in place in any direction before going back to the start of the main loop.

### Experimental set-up

The photormone was projected with an Epson EX9200 projector onto an acrylic sheet with a translucent top, which served as the surface on which the RAnts are operating. The projector uses three-chip digital light processing (DLP) which is required for the light sensors in the RAnts to pick up the photormone field. Tests with single-chip DLP projectors generated large noise in the light sensors and phototaxis was not possible. The dynamics of the photormone field is a function of the RAnt's positions and is given by

$$\partial_t c = D\nabla^2 c - k_M c + k_P \sum_{i=1}^n \mathcal{N}(r_i, \Sigma) \quad (17)$$

with  $c = c(\mathbf{x}, t)$  the photormone concentration at position  $\mathbf{x} = [x, y]$  and time  $t$ ,  $D = 10^{-5} \text{ m}^2 \text{ s}^{-1}$  the diffusion coefficient,  $k_M = 1 \text{ s}^{-1}$  the decay rate,  $k_P = 6.5 \text{ s}^{-1}$  the photormone production rate,  $n$  the number of RAnts detected in the arena,  $\mathcal{N}(r_i, \Sigma)$  a bivariate normal distribution with the position of the  $i$ th RAnt  $r_i$  as the mean and covariance  $\Sigma$  with diagonal entries  $\sigma^2 = 10^{-4} \text{ m}^2$ . The position of the RAnts are used as the centers of sources of photormone. If a RAnt is not moving, photormone is built up with rate  $k_P$  at that location over time and diffuses out. When the RAnt moves to a new location, the built up photormone decays with rate  $k_M$ . The reasoning for the parameter choices is as follows. The parameters were tuned

790  
791  
792  
793  
794  
795  
796  
797  
798  
799  
800  
801  
802  
803  
804  
805  
806  
807  
808  
809  
810  
811  
812  
813  
814  
815  
816  
817  
818  
819  
820  
821  
822  
823  
824  
825  
826  
827  
828  
829  
830  
831  
832  
833  
834  
835  
836  
837  
838  
839

to allow for a RAnt located at one position for one second to leave a detectable trace for 5 seconds. During that time, another RAnt moving at base speed  $v_b \approx 5\text{cm/s}$  can travel half the diameter of the arena. The diffusion length over the decay time scale is  $\approx 3\text{mm}$  which may appear small, however, RAnts are not always moving at base speed but often located in a particular location for multiple seconds to even minutes. The parameter choice described here has shown to neither saturate the domain with photormone nor be too volatile, but allowing the photormone to act as a spatiotemporal memory for the RAnts over the course of an experiment.

The positions of the RAnts are tracked with a webcam mounted above the arena and evaluated in Matlab. Blue markers are attached on the centroid of the case's upper surface which allow to use a simple blob detection to identify the pixel position of the RAnts. The photormone concentration is then dynamically updated in the same Matlab script and displayed on the RAnt arena with the projector. The tracking and integration of the photormone field is executed in real time which restricted the update rate of the projected field to 8 Hz on average. The low refresh rate did not have any noticeable consequences for the conducted experiments but might have affected results for RAnts with a much larger base speed and more volatile photormone dynamics.

The set-up of the enclosure for the RAnts consisted of approximately 200 wall elements arranged in three concentric circles where the outermost circle had a diameter of 50 cm. The outermost circle was prevented from being pushed outward from their initial position by a thin plastic ring that was attached to the base of the arena. The plastic ring was thick enough to prevent wall elements from leaving the confinement, but thin enough for RAnts to roll over it to escape the arena. For every experiment we randomly placed the rants in the arena and waited for the first RAnt to excavate out or the time limit of 15 minutes to be reached. At that point, data was stored and the experiment ended. Most experiments required no intervention, but in case of an empty battery of a RAnt or any unexpected critical failure during the experiments, we had two RAnts standing by to replace the defective RAnt. Since all RAnts are identical and the main memory is communicated through the environment and the photormone concentration, a switch has no further statistical consequences on the outcome of the experiments. There was no leader and no dedicated roles, which makes every RAnt replaceable.

We conducted experiments for five cooperation parameters  $C = \{0, 0.25, 0.5, 0.75, 1\}$  at fixed excavation rate  $E = 1$  and repeated experiments five times for each parameter. Every RAnt's software was updated before a new set of five experiments with the same cooperation parameter was conducted. For every experiment, we stored the webcam data and time stamps. The video frames were post-processed and locations of all RAnts and wall elements were stored as a function of time.

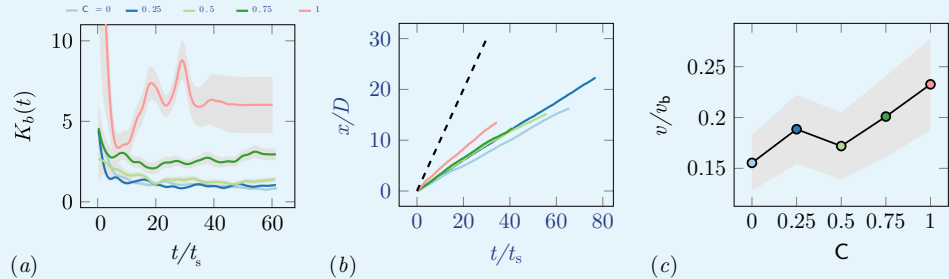
For the phase diagram experiments we used the previous data for cooperation parameters  $C = 0$  and  $C = 1$  for partial tunneling and tunneling, respectively. To induce jamming behavior and diffusion behavior the excavation rate had to be changed in the internal programming of the RAnts. By setting the excavation rate  $E = 0$  the probability of the magnet engaging vanished which led to jamming for high cooperation parameters, and diffusion for low cooperation parameters. We only collected data for two trials of a few minutes each in the diffusion and jamming case as tunneling cannot be initiated with disengaged magnets which reduces the timescales over which the behavior occurs.

### Cooperation parameter

We explored the effect of cooperation parameters on the excavation time and excavation performance as stated in the main text. Five cooperation parameters, i.e.  $C = \{0, 0.25, 0.5, 0.75, 1\}$ , were selected each of which was tested in five RAnt experiments with five RAnts. SI **Figure 3**

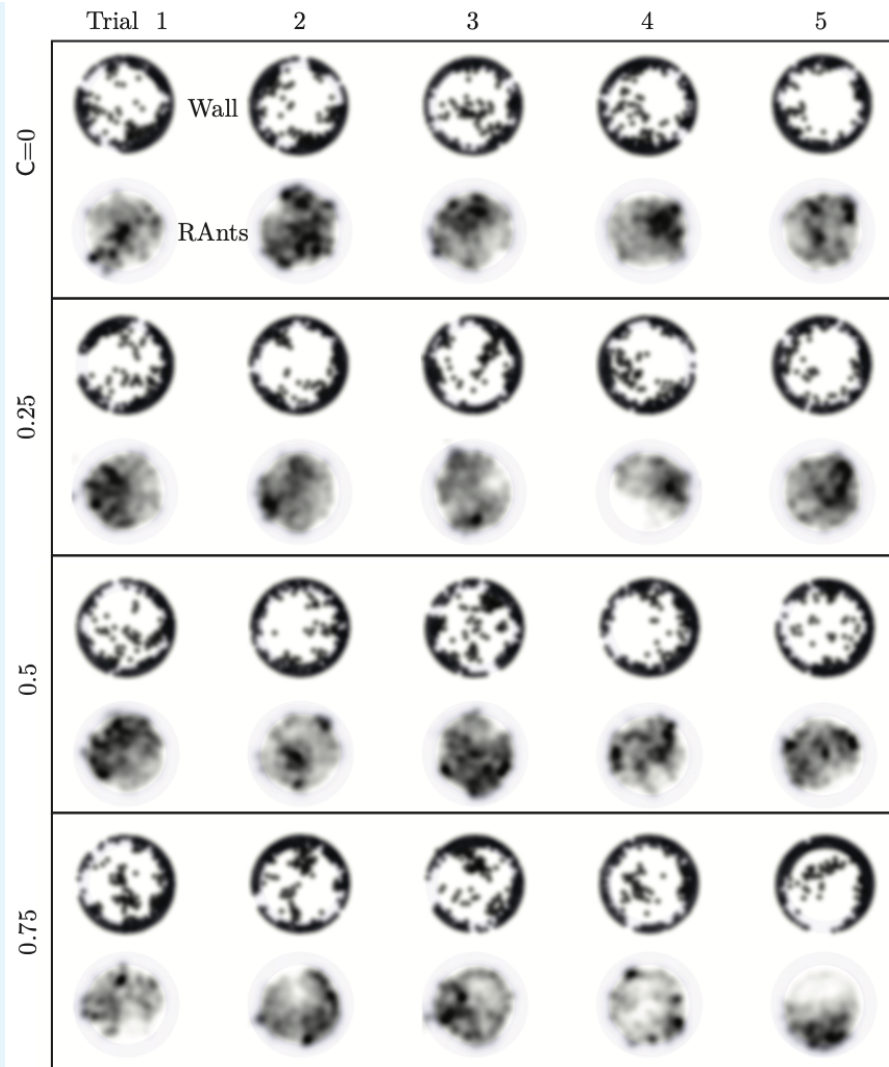
shows the final wall element distribution and the RAnt density averaged over the whole trial for all the conducted 25 experiments.

From the final wall element distribution one can deduce the degree of focus during the tunneling effort. For low cooperation parameters the initial three layers are excavated at multiple excavation sites. As the cooperation parameter increases, less excavation sites are visible and at  $C = 1$  there is in general only one large excavation site.



**Appendix 3 Figure 2.** (a) Von Mises concentration parameter,  $K_b$ , of the angular position of the excavated boundary elements as a function of time for different cooperation parameters and averaged over 5 experiments per cooperation parameter. (b) Total travelled distance of RAnts for different cooperation parameters. The travelled distance  $x$  is scaled by the size of the arena  $D$ . The dashed line shows the travelled distance of a RAnt moving at base speed  $v_b$  constantly. (c) RAnts' averaged speed  $v$  normalized by  $v_b = D/t_s$  for different cooperation parameters  $C$ .

While the final wall distribution shows only a snapshot in time, the RAnt distribution is averaged over time and therefore displays where the RAnts were mostly located throughout the run. At low cooperation numbers, the RAnt density is generally distributed all across the arena. Localization of the density toward one region was observed for low cooperation parameters as excavated wall elements were forming a new boundary that confined the RAnt motion to that region (see e.g.  $C = 0$  T4,  $C = 0.25$  T4). As the cooperation number increases, more distinct localized density becomes apparent. Due to the photomone field Rants operating at higher cooperation parameter values are more likely to start excavating in locations where RAnts have previously been present. The location of that attracting field is not known a priori, but emerges spontaneously through the interaction with other RAnts. The location of the peak density field at higher cooperation numbers strongly correlates with the point of excavation in the wall. The difference in RAnt behavior as a function of the cooperation parameter is the degree of focus during excavation as represented by the von Mises parameter of the angular position of excavated boundary elements shown in ??(a). A large value of the parameter indicates a high degree of concentration of the excavation effort, while low values indicate a scattered distribution of many digging sites. Another metric to assess the behavioral difference induced by the cooperation parameter is the traveled distance of the RAnts. SI **Figure 2** (b) displays the total travelled distance of a rant  $x$  normalized by the arena diameter  $D$  as a function of the normalized time  $t/t_s$ , where  $t_s = D/v_b$  and  $v_b$  the base speed, shows that RAnts travel a greater distance in the same amount of time at higher concentration parameters. The theoretical limit of the travelled distance is shown with the dashed line in the left-hand side figure, reflecting that RAnts do not constantly move at base speed, but are interrupted by other RAnts, obstacles, and fetching/dropping manoeuvres. As shown in SI **Figure 2** (c), RAnts travel at about a fifth of the base speed on average. An increase of the average speed is observed as a function of the cooperation parameter, which can be explained by the fact that obstacles are more scattered at lower cooperation parameters, effectively reducing the mean free path of a RAnt.



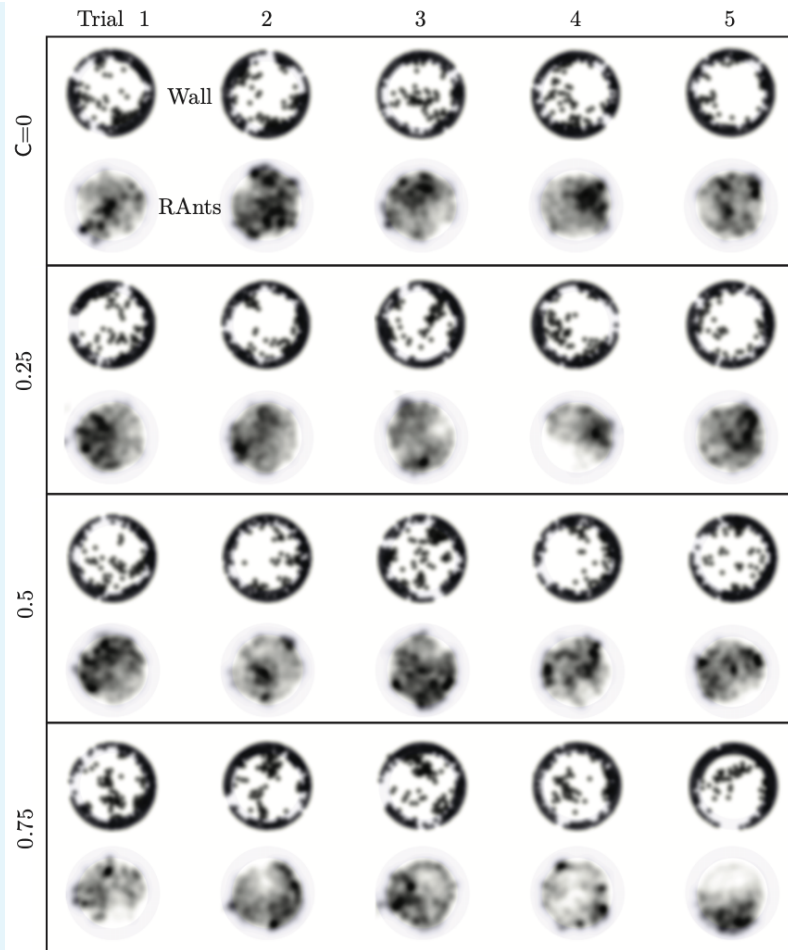
885  
886  
888

**Appendix 3 Figure 3.** Final wall element distribution and averaged RAnt density field (in units of  $\#/cm^2$ ) over the full duration of the run for all 20 experiments.

889  
890  
891  
892  
893  
894  
895  
896

### RAnt density

In our main result we used five RAnts to explore cooperative excavation in an artificial system. More RAnts than five hindered the excavation behavior as fellow RAnts would block each others path or disturb a RAnt during the fetching and deposition of wall elements. Fewer RAnts did manage to excavate out, but the excavation rate is slower and the spontaneous formation of an excavation site due to accumulation of photormone occurs later if at all. SI **Figure 4** shows the final wall element positions and RAnt density field averaged over time for  $C = 1$  and two experiments with one RAnt and two experiments with three RAnts.



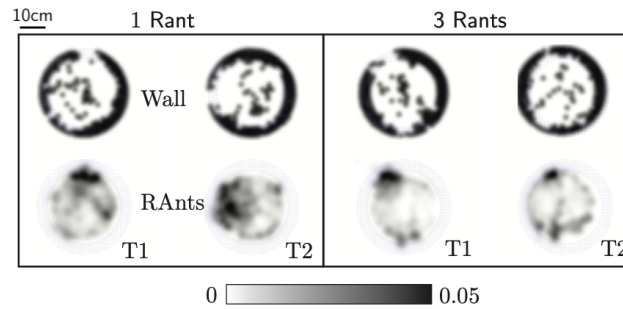
897  
898  
899  
900  
901  
902  
903  
904  
905  
906  
907  
908  
909  
910  
911  
912  
913  
914  
915

**Appendix 3 Figure 4.** Final wall element distribution and averaged RAnt density field (in units of  $\#/cm^2$ ) over the full duration of the run for experiments with one and three RAnts. The cooperation parameter was set to  $C = 1$  and the experiments was repeated twice (Trials T1 and T2).

A single RAnt can efficiently excavate a site if an initial photormone seed is present, but it is not robust. In fact, even though the RAnt in T2 managed to remove some elements in the last layer, it never excavated out but lost the photormone seed where it was digging and started diffusing again. Three rants were more successful in generating an initial photormone seed, but excavation occurred at multiple sites even for  $C = 1$  since the lower number of RAnts did not generate one dominating photormone field.

### Phases of cooperation in RAnts

In the RAnt case we can infer the phase in which the RAnts operate by looking at the tunnel size,  $1/K_b(t)$  and the location along the boundary at which the RAnts are localized,  $\rho_r(\phi)$  as they execute their task. We find that in the jammed and diffused phase there exists no tunnel and the variance remains zero throughout the process. However the location along the boundary  $\phi_b$  at which the RAnts spend their time the most has a large peak around the jammed location due to high cooperation which in the case of diffusion remains widespread (see ??).



916  
917  
918  
919  
920  
922

**Appendix 3 Figure 5.** From the RAnt experiments in *Figure 8*,  $K_b$  is the von Mises concentration parameter computed from the location of the boundary and  $\phi_r$  is the angular distribution of the RAnts in the arena averaged over time.  $\phi_b$  is the time-averaged mean azimuthal location of the RAnts in the arena. RAnts present over longer periods in a particular sector of the arena will cause a peak in  $\phi_r$ . One can infer the phase the RAnts are in by measuring these two quantities.

923  
924  
925  
926  
927  
928  
929

A successful tunnel, as we have already seen, has an initial increase in the variance that plateaus rapidly due to cooperation driven focus at a given location. As the RAnts are localized, focusing on their task, we again see peaks around the location of the tunnel. For a partial tunnel, due to low cooperation, the variance in the tunnel size is large and the location along the boundary the RAnts spend their effort is spread out. Thus the phase the RAnts operate in can be distinguished by using information about the environment, i.e. the tunnel size, in combination with agent dynamics, i.e. their location.